Association of the North Atlantic Surface Turbulent Heat Fluxes with Midlatitude Cyclones

NATALIA TILININA

Shirshov Institute of Oceanology, Russian Academy of Sciences, Moscow, Russia, and Alfred Wegener Institute, Helmholtz Centre for Polar and Marine Research, Bremerhaven, Germany

ALEXANDER GAVRIKOV AND SERGEY K. GULEV

Shirshov Institute of Oceanology, Russian Academy of Sciences, and Lomonosov Moscow State University, Moscow, Russia

(Manuscript received 6 October 2017, in final form 29 August 2018)

ABSTRACT

Atmospheric mechanisms leading to the formation of very strong turbulent air–sea heat fluxes in the North Atlantic are analyzed using the National Centers for Environmental Prediction (NCEP) Climate Forecast System Reanalysis (CFSR) for the winter periods from 1979 to 2010. Surface turbulent flux extremes were quantified by considering both absolute and relative extremeness of these fluxes. For all cases of very strong surface turbulent fluxes, regional composites of the associated atmospheric conditions were built using reanalysis output. These composites clearly demonstrate a critical role of the cyclone–anticyclone interaction zone in forming very strong surface fluxes. The implied importance of cyclones followed by anticyclones in generation of surface air–sea heat flux extremes was demonstrated by the analysis of case studies. We further used the results of numerical cyclone tracking to identify extratropical cyclones associated with air–sea flux events of different intensities and to quantify the life cycle characteristics of these cyclones. Analysis of frequency distribution of surface heat fluxes has shown that extreme fluxes over the North Atlantic are associated with less than 30% of winter cyclones and that this association occurs mostly during the initial stage of their life cycle. Analysis of life cycle characteristics of these cyclones shows, in turn, that they are considerably more intense than most North Atlantic cyclones and are characterized by rapid deepening and slower propagation. We argue that variability of the North American high is a key factor controlling atmospheric conditions favorable for the occurrence of high turbulent air–sea heat fluxes in the North Atlantic mid- and subpolar latitudes.

1. Introduction

Accurate estimation and identification of the mechanisms controlling air–sea heat fluxes in the mid- and subpolar latitudes are both critically important for diagnosing their role in ocean and atmospheric dynamics. In the North Atlantic, very high heat fluxes cause anomalous surface density fluxes, resulting in the surface transformation of water masses and associated deep convection of the Labrador and Greenland–Iceland–Norwegian (GIN) Seas (Moore et al. 2014; Holdsworth and Myers 2015 among others). Very strong sensible and latent heat fluxes over the western boundary currents (such as the Gulf Stream and Kuroshio) also impact the lower troposphere, modifying the low-level baroclinicity and thus affecting the dynamics of cyclones by which they were imposed in the first place (Giordani and Caniaux 2001; Nakamura et al. 2004; Bond and Cronin 2008; Kwon et al. 2010; Konda et al. 2010; Nakamura et al. 2012; Ogawa et al. 2012; Small et al. 2014; Ma et al. 2015b; DuVivier et al. 2016; Parfitt et al. 2016, 2017). Surface fluxes in the western boundary currents can also lead to local tropospheric moisture recycling, by forcing convective processes and precipitation (Minobe et al. 2008, 2010; Sasaki et al. 2012; Chechin et al. 2013; Pfahl et al. 2014; Hand et al. 2014; Vannière et al. 2017). A number of ocean modeling studies have demonstrated the impact of surface turbulent fluxes in the lower atmosphere at mesoscales and submesoscales (Small et al. 2008, 2014; Ma et al. 2015a; Parfitt and Czaja 2016; Bishop et al. 2017).

Supplemental information related to this paper is available at the Journals Online website: https://doi.org/10.1175/MWR-D-17-0291.s1.

Corresponding author: Natalia Tilinina, tilinina@sail.msk.ru

DOI: 10.1175/MWR-D-17-0291.1

Turbulent surface heat fluxes over the midlatitude oceans are highly variable. On synoptic scales and mesoscales, the heat flux changes over the periods from several hours to a few days can easily amount to several hundred watts per meters squared ($W\,m^{-2}$; Moore and Renfrew 2002; Yau and Jean 1989; Zolina and Gulev 2003; Ma et al. 2015b). This variability is much stronger than that on the seasonal and interannual time scales, where the surface flux variations are typically an order of magnitude smaller (Zhao and McBean 1986; Yu and Weller 2007; Shaman et al. 2010; Gulev and Belyaev 2012; Gulev et al. 2013), which underscores the need for identifying the mechanisms of such short-term synoptic variability of the surface turbulent heat fluxes.

Many diagnostic studies have demonstrated that very strong turbulent heat fluxes in the midlatitudes are associated with rapidly moving cyclones over the highly inhomogeneous ocean (Fleagle et al. 1988; Neiman and Shapiro 1993; Alexander and Scott 1997; Zolina and Gulev 2003; Clayson and Bogdanoff 2013; O'Reilly and Czaja 2015; Ma et al. 2015b). The formation of very strong and extreme surface fluxes there is thought to be associated with cold air outbreaks whereby extremely cold and dry air in the rear parts of cyclones is advected to relatively warm surface regions (Neiman and Shapiro 1993; Rudeva and Gulev 2011; Moore et al. 2014; Bond and Cronin 2008; Papritz et al. 2015; Kim et al. 2016). The most intense cold air outbreaks occur because of the cyclones moving along the main North Atlantic storm track over the Gulf Stream, Labrador Sea, and GIN Seas. Such cyclones and the related cold air outbreaks are less frequent over the central and eastern North Atlantic (Kolstad et al. 2009), which amounts to the lower climatological turbulent fluxes there caused by the absence of favorable land–sea or ice–sea contrasts that could lead to the advection of very cold air masses over the warm ocean.

However, not all of the midlatitude cyclones are associated with strong surface turbulent heat fluxes. Rudeva and Gulev (2011) demonstrated that over the North Atlantic midlatitudes, only 43% of cyclones provided higher than average surface heat fluxes. This finding is consistent with the work of Yuan et al. (2009) and Patoux et al. (2009), who found that in the Southern Ocean most of the heat loss occurs outside of the storm-track regions. While the concept of copropagation of sea level pressure (SLP) disturbances and synoptic anomalies of surface fluxes is widely accepted (Alexander and Scott 1997; Zolina and Gulev 2003), there is no direct evidence of high correlation between the cyclone activity and the variability of surface turbulent fluxes on interannual time scales. Some regional association between the two for selected individual winters was demonstrated in the North Atlantic by Woollings et al. (2016). Papritz et al. (2015) considered wintertime fluxes in the high-latitude South Pacific and demonstrated that at interannual time scales an enhanced (reduced) cyclone frequency is associated with an enhanced (reduced) frequency of cold air outbreaks west of the climatological cyclone frequency maxima, with the corresponding modulation of the surface heat fluxes. Recently, Ma et al. (2015b) concluded that the occurrence of extreme flux events is closely related to the variability associated with large-scale circulation patterns, such as the Aleutian low pattern and the east Atlantic pattern for the Kuroshio and Gulf Stream regions, respectively. This work, as well as the studies of Alexander and Scott (1997) and Zolina and Gulev (2003), however, analyzed the atmospheric and surface flux conditions using bandpass filtering of the requisite oceanic and atmospheric fields, and no attempt was made to relate surface heat fluxes of different intensity to the individual cyclones.

In this study, we aim to understand the mechanisms of the synoptic variability of turbulent surface heat fluxes in the midlatitudes by quantifying the atmospheric circulation conditions associated with surface fluxes of different intensities. Specifically, we address two important questions: (i) What are the atmospheric synoptic conditions associated with the occurrence of strong turbulent surface heat fluxes over the North Atlantic? (ii) What is the role of extratropical cyclones in the formation of such conditions? Using high-resolution fluxes and flux-related state variables from the National Centers for Environmental Prediction (NCEP) Climate Forecast System Reanalysis (CFSR), we relate strong turbulent heat fluxes over the North Atlantic to the corresponding synoptic circulation patterns, cyclone trajectories, and cyclone life cycle characteristics.

The paper is organized as follows. Section 2 describes the data and analysis methodology. Section 3 presents the statistics of very strong turbulent fluxes in the North Atlantic midlatitudes and analyzes their role in large-scale air–sea heat exchange. In section 4, we relate the occurrence of surface heat fluxes of different intensities to the requisite atmospheric synoptic conditions. Section 5 proceeds with an analysis of the cyclone life cycles associated with surface heat flux events of different magnitude. Section 6 discusses our results in the context of the large-scale circulation patterns responsible for the occurrence of very strong and extreme air–sea fluxes.

2. Data and methods

a. *NCEP CFSR*

The NCEP CFSR system (Saha et al. 2010) utilizes a T382 coupled atmosphere–ocean–land surface–sea ice

model for the generation of the 6-h first-guess field that aims to resolve the air–sea interaction processes with a higher accuracy than in the uncoupled models. CFSR uses a three-dimensional variational (3D-Var) data assimilation algorithm with a refinement provided by the First Order Time interpolation to the Observation (FOTO; Rancic et al. 2008). CFSR couples the atmosphere, simplified ocean, and sea ice models to generate 6-hourly first-guess fields. Compared to the other modern reanalysis datasets, the NCEP CFSR dataset was found to adequately reproduce cyclone activity over the Northern Hemisphere (NH) (Allen et al. 2010; Hodges et al. 2011; Tilinina et al. 2013). The synoptic- and subsynoptic-scale variability of the turbulent fluxes in the NCEP CFSR dataset are in general agreement with the other products, such as the ERA-Interim and MERRA, in terms of its magnitude and temporal behavior (Roberts et al. 2012; Bentamy et al. 2017). Ma et al. (2015b) and O'Reilly et al. (2017) demonstrated utility of the NCEP CFSR reanalysis in establishing the association of strong fluxes with atmospheric conditions.

We analyzed the NCEP CFSR output on a 0.5° grid with 6-hourly temporal resolution for Januaries over the period from 1979 to 2010. For our analysis, we used the 6-hourly accumulated latent and sensible heat fluxes diagnosed by the reanalysis to derive the total turbulent (latent plus sensible) heat flux (LSHF); we also utilized the data for 6-hourly SLP, 10-m zonal (U), and meridional (V) components of the wind, 2-m air temperature (T2M), sea surface temperature (SST), as well as 2-m specific humidity (H2M) and sea ice concentration.

Compared to the other modern reanalysis datasets, the NCEP CFSR dataset was found to adequately reproduce the cyclone activity over the NH (Allen et al. 2010; Hodges et al. 2011; Tilinina et al. 2013). The synoptic and subsynoptic variabilities of the turbulent fluxes in the NCEP CFSR dataset are in a general agreement with the other products, such as the ERA-Interim and MERRA, in terms of its magnitudes and temporal behavior (Roberts et al. 2012; Bentamy et al. 2017). Note that Ma et al. (2015b) and O'Reilly et al. (2017) also used the NCEP CFSR to establish the association of strong fluxes with atmospheric conditions.

For case-study diagnosis, we also used high-resolution meteorological data (SLP, wind speed, SST, and air temperature) from the NOAA National Data Buoy Center (NDBC) buoy 41048 located in the Gulf Stream at 31.868°N, 69.590°W (Fig. 6a). The buoy wind speed measurements were obtained by an hourly accumulation of 8-min averages, with anemometer height at 5 m above the sea level; the air temperature measurements were at 4 m above the sea level, and the SST was measured at 0.6 m below the sea level.

b. *Cyclone tracking*

Cyclone tracking over the NH was performed using the numerical algorithm of Zolina and Gulev (2002, 2003). This algorithm interpolates the original NCEP CFSR SLP fields onto a 181×181-point polar orthographic projection grid (Zolina and Gulev 2002) using the modified method of local procedures (Akima 1970). The cyclone-tracking algorithm incorporated a dynamical interpolation of SLP fields onto a finer time grid for proper detection of cyclone step-by-step migrations. Cyclone centers were identified by iterative analysis of the local SLP spatial derivatives. Building the cyclone trajectories relied on the method of the nearest neighbors with further three-pass analysis of the cyclone propagation velocities, as well as on the procedures that dealt with the crossing trajectories. The output of the tracking (cyclone coordinates, central pressure, and time of occurrence) was subjected to postprocessing, which included minimum thresholds of 1 day for the cyclone lifetime, 1000 km for the cyclone migration distance, and 1500 m for the orography elevation applied to all tracks. The maps of cyclone numbers and frequencies (when appropriate) were constructed on a 2° regular grid by computing the cyclone occurrences within circular cells with the surface area of 155 000 km^2 centered at each grid point, using the methodology of Tilinina et al. (2013).

From the output of the cyclone tracking, we estimated the parameters of the cyclone life cycle such as the minimum SLP over the cyclone lifetime, the mean and maximum deepening/filling rates (dP and $dP_{\max}$, respectively), the cyclone propagation speed, and the cyclone lifetime. Our present numerical methodology was extensively evaluated during the Intercomparison of Mid-Latitude Storm Diagnostics (IMILAST) project (Neu et al. 2013; Rudeva et al. 2014) and proved to have a comparable or better skill in capturing the cyclone characteristics compared to other available cyclone-tracking algorithms. This method was also successfully applied for the comparative assessment of the cyclone activity in different reanalysis datasets (Tilinina et al. 2013, 2014), in operational products of different resolutions (Jung et al. 2006), in climate model simulations (Löptien et al. 2008; Ulbrich et al. 2013; Semmler et al. 2016), and in the idealized atmospheric models (Kravtsov and Gulev 2013; Kravtsov et al. 2016).

c. *Composite analysis of the atmospheric conditions associated with surface flux events of different intensities*

To link turbulent heat fluxes of different intensities to atmospheric synoptic circulation patterns, we adapted the compositing methodology of Rudeva and Gulev (2011),

originally developed for the analysis of cyclones at different stages of their life cycles. In contrast to the work of Rudeva and Gulev (2011), however, we computed the composites of various atmospheric parameters conditioned on the magnitude of air–sea turbulent heat fluxes (e.g., for very strong fluxes corresponding to >80th percentile of their empirical distribution). Thus, we do not explicitly assume preexistence of a cyclone in our analysis but instead focus on composites comprising all possible kinds of synoptic conditions associated with surface heat fluxes in a given range of intensities.

We defined the classes of heat flux events of different intensities based on one-dimensional empirical cumulative distribution function (CDF) accumulated over the entirety of the LSHF dataset (i.e., utilizing every available observation at every grid point). In most analyses we considered three ranges of surface heat fluxes: weak LSHF with values below the 20th percentile of the flux CDF, moderate LSHF (values between 40th and 60th percentiles), and strong fluxes exceeding 80th percentile of the CDF. Using the empirical CDF, rather than its theoretical version (Gulev and Belyaev 2012) is adequate for our purposes, since we do not specifically focus on the most extreme heat fluxes in the tails of the probability density function. Next, for every available LSHF snapshot, we found the areas exhibiting the weak, moderate, or strong fluxes. For example, Fig. 1a shows snapshots of different meteorological fields in the North Atlantic region at 1200 UTC 3 January 2008 along with four areas of strong surface heat fluxes (i.e., the areas in which the LSHF exceeds the 80th percentile of the empirical CDF).

For all such areas S of weak, moderate, or strong heat fluxes, we defined their equivalent centers of mass (CM) (see Fig. 1) whose coordinates were computed as follows:

$$\begin{pmatrix}\varphi_{\mathrm{CM}}\\ \lambda_{\mathrm{CM}}\end{pmatrix} = \iint_S \begin{pmatrix}\varphi\\ \lambda\end{pmatrix} \mathrm{LSHF}(\varphi,\lambda)\, d\varphi\, d\lambda / \langle \mathrm{LSHF}\rangle_S = \sum_{i=1}^{n} \begin{pmatrix}\varphi_i\\ \lambda_i\end{pmatrix} r_{fi}, \quad (1)$$

Here φ_{CM} and λ_{CM} are the latitude and longitude of the CM, φ_i and λ_i are the latitudes and longitudes of the ith grid point contained within the area S, n is the total number of grid points within the area S, $\langle \mathrm{LSHF}\rangle_S$ is the average value of the LSHF over the area S, and r_{fi} is a weighting function given, for the ith grid point by the following expression:

$$r_{fi} = \frac{\mathrm{LSHF}_i(\varphi_i,\lambda_i)}{\langle \mathrm{LSHF}\rangle_S}, \quad (2)$$

where LSHF_i is the value of the LSHF at the ith grid point within the area S.

For our composite analysis, we interpolated various meteorological quantities onto a new rectangular, equally spaced, 74-km resolution 81×81 (x, y) grid centered at the location of a given center of mass $(\varphi_{\mathrm{CM}}, \lambda_{\mathrm{CM}})$, using the method of local procedures (Akima 1970); in displaying the composite maps, we only show the fields within the circular area inscribed in the original square region. The meteorological quantities we considered included LSHF, atmospheric state variables (temperature, humidity, wind speed, and SLP), as well as some derived quantities: vertical temperature difference δT = SST − T2M, where SST is the sea surface temperature and T2M is 2-m air temperature, and vertical humidity difference δE = 0.98QS − Q2M, where QS is the saturation specific humidity at sea surface temperature with the correction coefficient of 0.98 accounting for surface salinity, and Q2M is the 2-m atmospheric specific humidity. Figures 1b,c show examples of such interpolation for LSHF, wind speed and SLP corresponding to CM locations within the Gulf Stream (Fig. 1b) and the Labrador Sea (Fig. 1c). Note that while technically this interpolation procedure is similar to that of Rudeva and Gulev (2011), our approach is conceptually different: Rudeva and Gulev (2011) were building *cyclone composites* for the analysis of cyclone life cycles, whereas here we aim to build the *composites of the atmospheric environmental conditions* associated with turbulent surface heat fluxes of different intensity.

We computed the composites of all of the meteorological fields defined above on the local CM centered grid, for each of the three heat flux intensity classes (i.e., weak, moderate, and strong). In doing so, we only considered the areas larger than 125 600 km^2 (which is equivalent to the area of a circle with the radius of 200 km). We also differentiated between the heat flux areas with CM locations belonging to five different geographical regions, as shown in Fig. 2a. Figure 2b shows the probability distribution of the areas (10^6 km^2) of LSHF flux regions corresponding to the moderate surface heat flux conditions, for the five different regions. The largest areas are found in the central North Atlantic and Gulf Stream, with median values of approximately 2 000 000 km^2. Over the Labrador Sea and GIN Seas regions, the areas are smaller, being as small as 500 000 km^2 in the 85% and 45% of the total number of cases, respectively, which can be explained by the smaller overall sizes of Labrador Sea and GIN Seas regions (Table 1).

Table 1 lists the total number of cases, over the 1979–2010 period, which were averaged to produce the

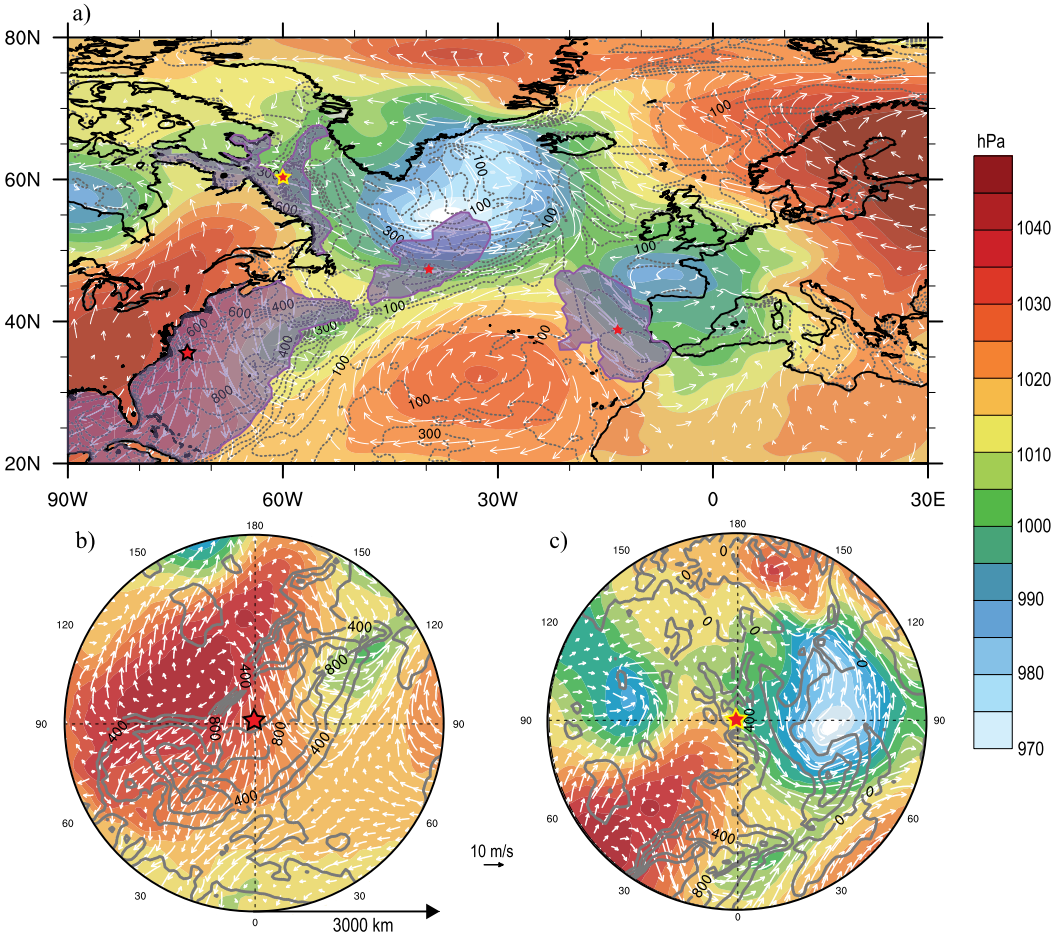

FIG. 1. (a) Snapshot of the SLP (color shading), LSHF (contours), and surface wind vectors (white arrows) from NCEP CFSR at 1200 UTC 3 Jan 2008. Overlaid areas (purple shading) correspond to the LSHF exceeding the 80th percentile of probability distribution at every grid point for January (1979–2010). Red stars mark the "mass centers" of these LSHF areas, computed from Eq. (1). (b),(c) SLP (color shading), LSHF (contours), and wind vectors fields interpolated onto the new coordinate system with the virtual pole at the mass center of the corresponding areas of LSHF exceeding the threshold for the locations over (b) the Gulf Stream and (c) the Labrador Sea [shown in panel (a) by red stars].

composites for different regions and for each magnitude of LSHF. Note that these numbers reflect the combined effect of the frequency of occurrence of weak, moderate, or strong surface heat fluxes in *both space and time*, since the actual locations of the corresponding areas are not fixed even within a given geographical region. (See Fig. S1 in the online supplemental material for further details and discussion of our compositing methodology.) Note also that the effective number of statistical degrees of freedom in each composite may in fact be smaller than the number of cases that were averaged to produce this composite, since some of the consecutive events may not be statistically independent. For instance, 49 events on average for LSHF > 80th percentile in the Labrador Sea may consist of several series, each represented by events that persist during several consecutive 6-hourly time steps. These events are therefore not independent of each other.

Our analysis (Fig. 3) shows that the average monthly number of independent events corresponding to the strong fluxes is 14.7 events per month, with 55% of them lasting less than 18 h. The highest number of independent events (54.8 events per month) was found in the GIN Seas for the moderate fluxes (40th to 60th percentile of the LSHF CDF). These events are also characterized by the shortest durations (~70% of events last less than 12 h), consistent with the estimates of cyclone lifetimes for this region (e.g., Gulev et al. 2001; Rudeva and Gulev 2011). Over the Gulf Stream and eastern North Atlantic, a typical series of consecutive heat flux events tends to be longer (60% of events last more than 12 h for the strong fluxes exceeding 80th percentile), but

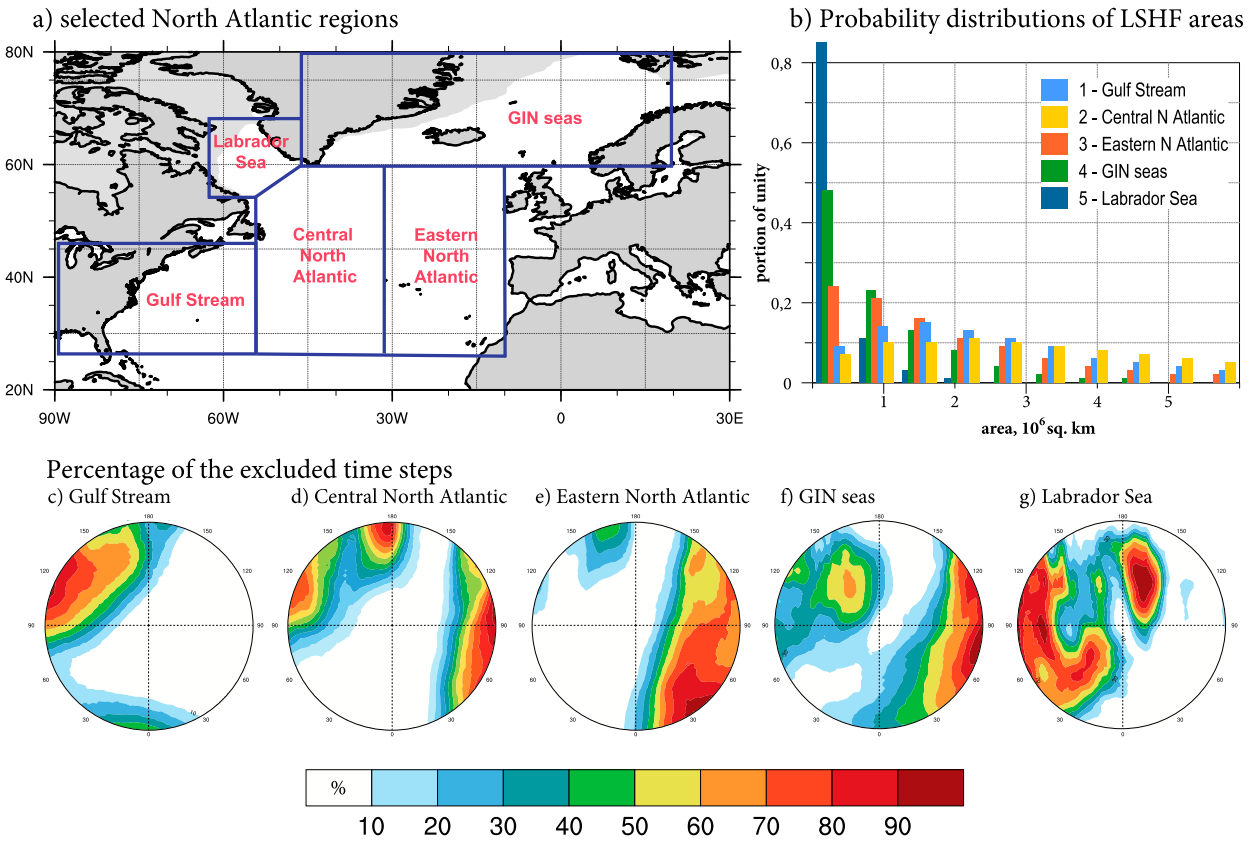

FIG. 2. (a) Regions in the North Atlantic for which composites were built, (b) probability distributions of the areas inside LSHF contours corresponding to the 40th–60th percentile of surface flux for different regions, (c)–(g) distributions of the percentage of the time steps for each grid point of the 40th–60th percentile composites, which were excluded from compositing ocean-related variables (LSHF, δT, δE) as they fall to the land areas from NCEP CFSR, Januaries 1979–2010.

the average number of independent events is lower, at 36.5 independent events per month.

Events characterized by short durations (e.g., less than 18 h) may occur because of short-term weakening of surface fluxes below a certain percentile. One potential mechanism for achieving such weakening could be associated with diurnal cycle. However, our analysis (not shown) refutes this hypothesis, indicating instead that short episodes of the occurrence of a heat flux with a given magnitude most likely result from subsynoptic variability of the surface fluxes. To account for the effect of such short-duration events we also considered, in section 4b, the composites based on the events lasting longer than 18 h, which reduced the number of composite members by 50%–80% (see Fig. 3); the total number of composite members corresponding to these longer events (TOT18) is also shown in Table 1. Furthermore, to eliminate the biases associated with potentially interdependent heat flux occurrences within a given category, we also analyzed in section 4b the composites based on subsampling of cases within each event lasting longer than 18 h (IND18 in Table 1), with the resulting number of composite members being an order of magnitude smaller than with the original sampling.

We computed the SLP and wind composites over both the ocean and land regions, while the quantities related to air–sea interaction (LSHF, δT, and δE) were naturally restricted to the oceanic areas; the mechanisms forming the synoptic variability of the turbulent heat exchange over land are very different from those over the ocean and are not considered here. For the oceanic composites, the number of maps used to compute the composite-mean value of a given field is generally not uniform throughout the CM-centered interpolation region, since parts of this region may extend over land (Figs. 2c–g). For example, at the eastern boundary of the composites for the GIN Seas, up to 90% of the events were excluded from the compositing of LSHF, δT, and δE (Fig. 2f). In the resulting composites we therefore masked out the areas for which >80% of the cases were excluded from compositing because of occurrences over land.

TABLE 1. Number of the LSHF areas (composite members for Figs. 9–11, and supplemental Figs. S2 and S3) with flux values falling into different percentiles for the five regions (see Fig. 2a) for Januaries 1979–2010. Shown are the total numbers of composite members based on all 6-hourly time steps (TOT), total numbers of composite members based on all 6-hourly time steps for the events lasting longer than 18 h (TOT18), and number of independent composite members for the events lasting longer than 18 h (IND(18). Also shown are the areas of the five regions in km^2.

Region		Percentile range			Region area, km^2
		<20th percentile	40th–60th percentile	>80th percentile	
1—Gulf Stream	TOT	2217	2435	1943	5 923 012
	TOT (18)	1101	648	1215	
	IND (18)	134	107	150	
2—Central North Atlantic	TOT	2330	2624	2345	8 675 913
	TOT (18)	846	600	1271	
	IND (18)	122	92	158	
3—Eastern North Atlantic	TOT	1984	2496	2124	4 007 096
	TOT (18)	814	960	1192	
	IND (18)	107	137	142	
4—GIN Seas	TOT	3065	2755	3270	4 903 672
	TOT (18)	882	339	1376	
	IND (18)	134	59	168	
5—Labrador Sea	TOT	1507	1645	1568	964 341
	TOT (18)	666	492	799	
	IND (18)	89	75	103	

Finally, to complement composites of the atmospheric conditions, we derived a subset of cyclone tracks associated with LSHF events of different intensities. This procedure is described in detail in section 5.

3. Very strong and extreme turbulent heat flux events in the North Atlantic midlatitudes

Different diagnostic, observational, and modeling studies (Renfrew et al. 2002; Gulev and Belyaev 2012; Moore et al. 2014; Harden et al. 2015) reported a spread in estimates of extreme surface fluxes. Estimates of extreme fluxes derived from observations or using state-of-the-art bulk formulas (e.g., Fairall et al. 2003, 2011) can be as large as 1000–2000 W m^{-2} of both the sensible and latent heat fluxes in the regions of the western boundary currents and the subpolar latitudes. These estimates can depend strongly on the bulk parameterizations used (Bourassa et al. 2013; Brodeau et al. 2017) and can also vary across different reanalyses and satellite products (Bentamy et al. 2017). Earlier studies (Moore et al. 2014; Harden et al. 2015) used the 95th percentile to estimate the extreme fluxes in the Labrador Sea and the central Iceland Sea. In this paper, we define very strong fluxes as those exceeding 80th percentile of the empirical probability distribution and extreme fluxes as those exceeding the 95th percentile.

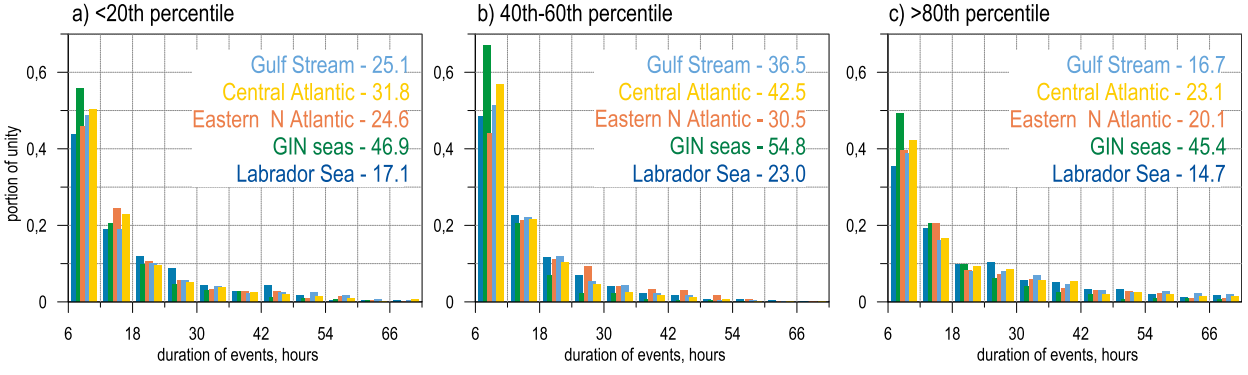

FIG. 3. Probability distributions of the durations (hours) of the independent LSHF events corresponding to different percentiles. Independent events were defined as the time slots when LSHF values are falling into the three ranges of empirical distributions: (a) weak fluxes <20th percentile, (b) moderate fluxes between the 40th and 60th percentiles, and (c) strong fluxes >80th percentile. Numbers in the legend indicate the average monthly number of the independent events.

The spatial pattern of the mean January LSHF for the period 1979–2010 (Fig. 4a) is consistent with the winter surface flux climatologies in the other reanalysis datasets (e.g., Gulev and Belyaev 2012) and with those in the blended products, such as OAFlux (Yu and Weller 2007) and CORE (Large and Yeager 2009). The highest wintertime mean LSHF amounted to 500 $W m^{-2}$ in the Gulf Stream and varied from 250 to 300 $W m^{-2}$ in the Labrador Sea. Figure 4b shows the mean values and maximum values of the 90th percentile of the LSHF for January of each year; both fields were computed over the entire 32-yr (1979–2010) period. The spatial pattern of the 90th percentile LSHF is similar to that presented by Gulev and Belyaev (2012). The maximum values of the 90th heat flux percentile in the Gulf Stream vary from 700 to 1000 $W m^{-2}$ and are as large as 850 $W m^{-2}$ in the Labrador Sea.

We also considered the fraction of the time-integrated (e.g., over month) heat loss caused by the fluxes exceeding a given percentile (relative extremes, Fig. 5a). The spatial pattern of the relative extremes is quite different from that of the mean (Fig. 4a) and absolute extremes (Fig. 4b). The highest relative contribution of extreme flux events occurs in the central midlatitudes and in the Iceland and Greenland Seas, where the top 10% of the distribution accounts for 40%–65% of the total monthly heat loss. In some years, this fraction can be higher than 90% and even reach 99%. In the areas of the strongest climatological and extreme fluxes (Gulf Stream, Labrador Sea) the relative extremes are smaller (20%–30% of the total LSHF is provided by flux events exceeding the 90th percentile). Note that in some subpolar regions, such as the Greenland Sea and the Grand Banks of Newfoundland, the contribution of very strong and extreme surface fluxes (e.g., of the fluxes exceeding 90th percentile) to the time-integrated totals locally reaches the values of larger than 80%. These estimates are in agreement with Papritz and Spengler (2017) who reported that 60%–80% of the heat loss over the GIN Seas in winter occurs because of cold air outbreaks. However, Fig. 5 shows that this contribution is lower (30%–40%) in the Labrador Sea, where the cold air outbreaks are also very pronounced (Kolstad et al. 2009; Moore et al. 2014). This can be partly explained by the smaller climatological values of the total turbulent heat flux (typically $<100 W m^{-2}$) over the Greenland Sea and the Grand Banks of Newfoundland compared to the Labrador Sea. Low climatological heat fluxes over the former regions result from the alternation of the episodes of extremely high turbulent fluxes with prolonged periods of near-zero or negative heat flux values, especially for the sensible heat flux.

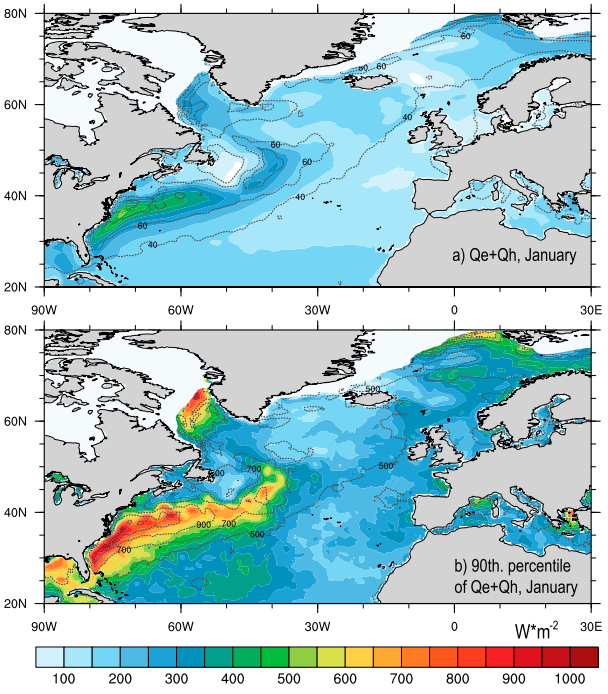

FIG. 4. (a) Climatological January LSHF (color shading) for the period 1979–2010 together with standard deviations (dashed contours), and (b) climatological January 90th percentile of the LSHF (color shading) along with maximum values of the 90th percentile of the LSHF (dashed contours) over the 1979–2010 period. White shading marks climatological January ice extent (15% concentration).

By contrast, the climatological LSHF over the Labrador Sea typically reaches 300–400 $W m^{-2}$ implying a smaller relative input of the episodes of strong and extreme fluxes to the long-term total.

Figures 5b and 5c show the dependences of the fractions of the latent (Fig. 5b) and sensible (Fig. 5c) heat loss caused by the events exceeding the different percentiles of the empirical surface heat flux CDF, from the 5th to 95th, for different regions. In the tropics, the relative extremes are the smallest for all the percentiles. The midlatitude regions are characterized by much higher contributions of very strong flux events to the time-integrated fluxes. The contributions of the events of different magnitudes to the total heat loss for sensible and latent fluxes are generally in a qualitative agreement. However, quantitatively, sensible fluxes demonstrate stronger relative extremeness, especially in the subpolar regions. Gulev and Belyaev (2012) also noted heavier tails for the probability distributions of sensible flux compared to the latent flux. In subpolar latitudes, the upper 15%–20% of the sensible heat flux distribution account for over 90% of the time-integrated total sensible heat loss, which is 20%–40%

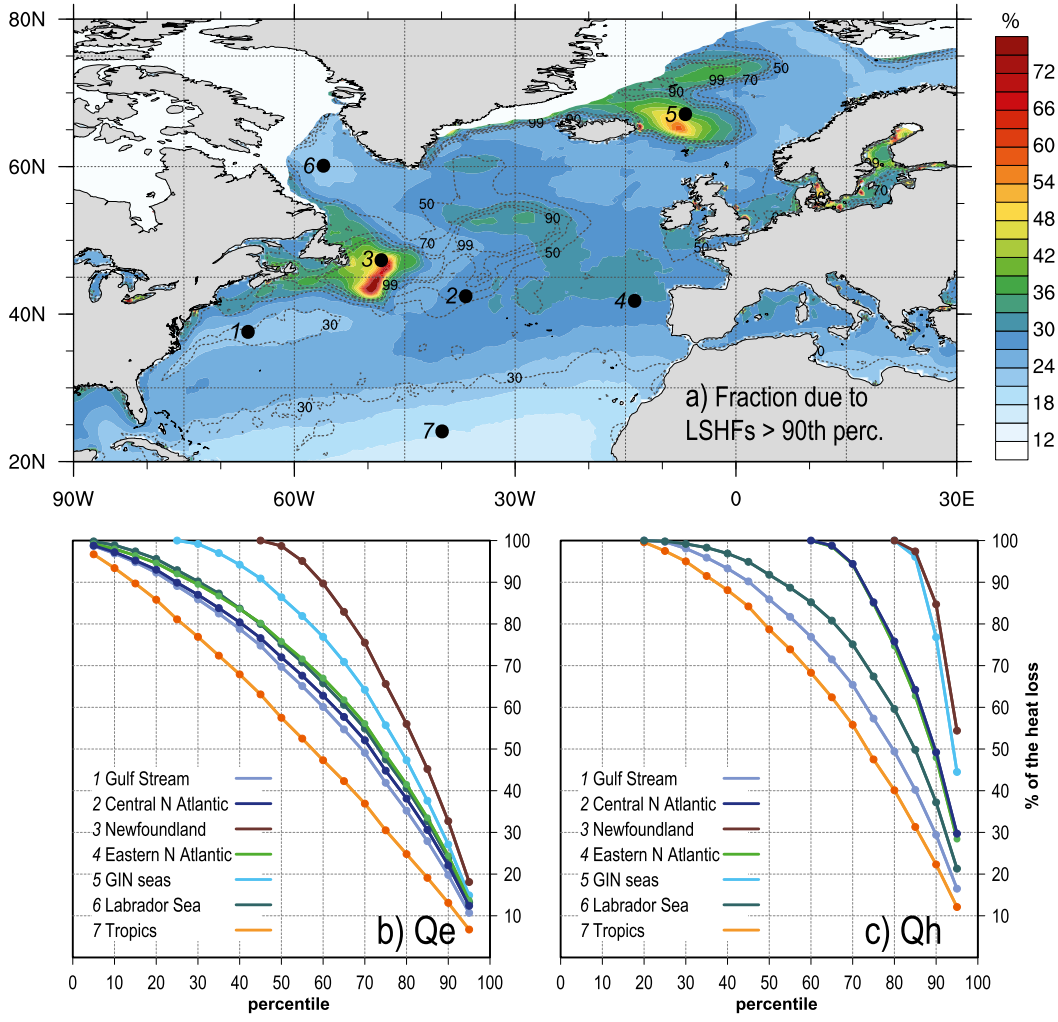

FIG. 5. (a) Climatological January relative extremeness (%) of LSHF represented by the fraction of time-integrated heat loss resulting from the LSHFs exceeding the 90th percentile for 1979–2010 (color shading) along with its maximum values (dashed contours) over the 1979–2010 period; (b),(c) dependences of relative extremeness (fraction of time-averaged heat loss, %) on the percentile of the (b) latent and (c) sensible heat flux distributions for different regions, indicated by numbered circles in (a). White shading in (a) marks climatological January sea ice extent (15% concentration).

higher than for the latent flux. A similar situation is observed in the central North Atlantic and in the Gulf Stream. For LSHF, the upper 25% of the distribution accounts for 90% of the total heat loss. The contribution of the upper 20% in different regions varies from 40% to nearly 100% for sensible flux and from 25%–55% for latent flux (Figs. 5b,c). Despite differences in magnitude, the spatial patterns of the relative extremeness for sensible and latent fluxes are very consistent. Point correlations between synoptic time series of sensible and latent fluxes can exceed 0.95 over the Gulf Stream and midlatitude regions, being on average close to 0.9 (not shown). In the remaining presentation, we will mostly analyze the total turbulent heat fluxes, LSHF; however, we will keep in mind different contributions of sensible and latent fluxes to strong air–sea heat exchanges in subpolar regions.

Our estimates of the contribution of very strong and extreme heat flux events to the total air–sea heat exchange are also consistent with the work of Shaman et al. (2010), who found that 40% of the heat loss in the North Atlantic in the winter occurs during 20% of the days, and with the work of Ma et al. (2015b), who reported a significant contribution of extremes to the net heat loss for both the North Atlantic and North Pacific. Overall, in the area between 30° and 70°N, approximately 30% of the total area-integrated LSHF is associated with episodes exceeding the 90th percentile, thus implying the

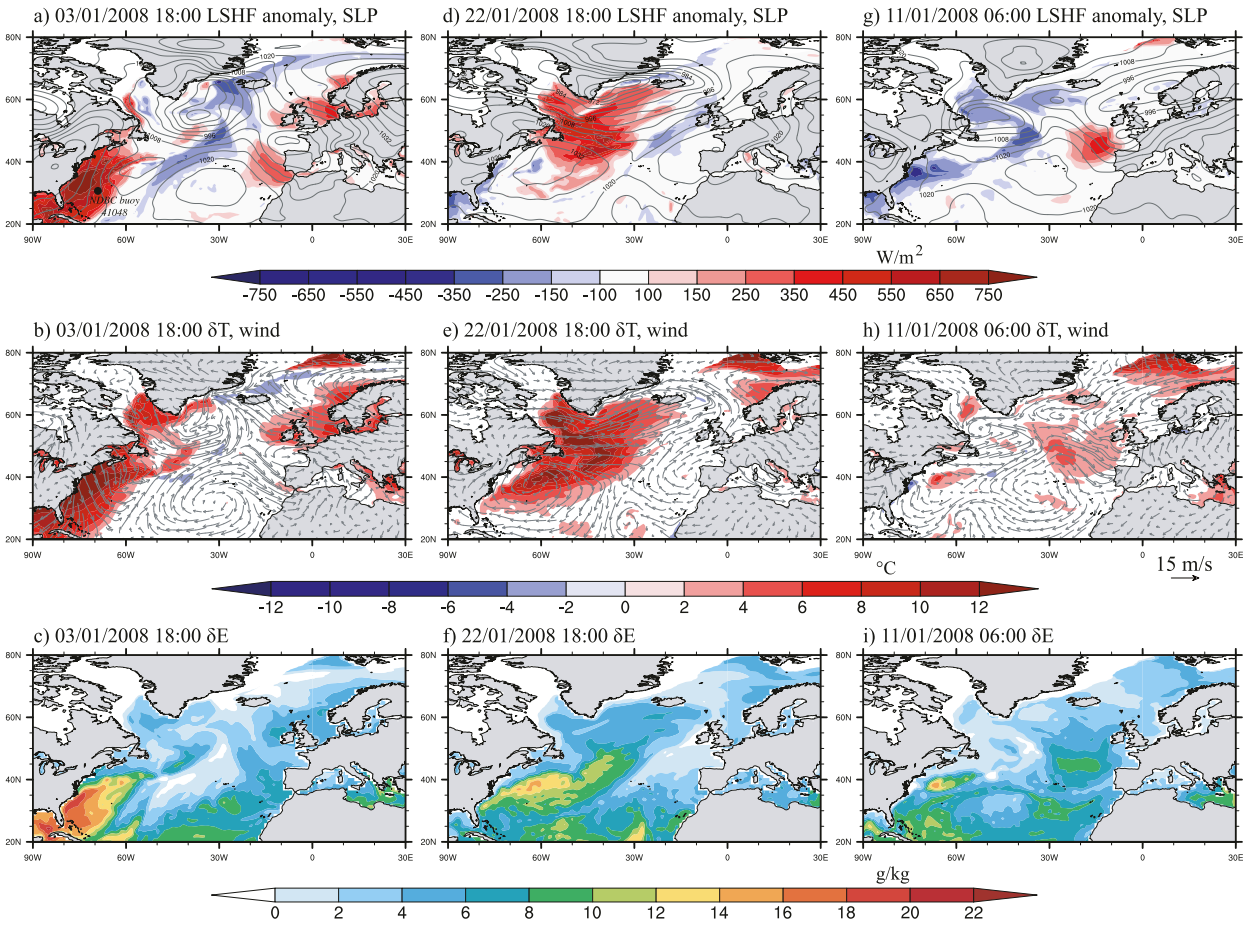

FIG. 6. Cases of association of LSHF of different magnitudes with atmospheric conditions for (a)–(c) 1800 UTC 3 Jan; (d)–(f) 1800 UTC 22 Jan; and (g)–(i) 0600 UTC 11 Jan 2008. In (a),(d),(g), color stands for LSHF anomalies ($W\,m^{-2}$) relative to January monthly mean and contours show SLP (hPa). In (b),(e),(h), color stands for δT (°C) and arrows for wind speed vectors. In (c),(f),(i), color stands for δE ($g\,kg^{-1}$).

important role of very strong surface fluxes in the surface ocean heat budget.

4. Association of surface fluxes with atmospheric synoptic conditions

a. Analysis of case studies

Figure 6 shows three cases of the association of synoptic LSHF anomalies (with respect to the monthly January mean) with SLP, as well as with δT, δE, and surface wind vectors, which determine the turbulent heat fluxes according to the bulk formulas. Two cases of very high positive LSHF anomalies exceeding $400\,W\,m^{-2}$ (equivalent to 1000–$1200\,W\,m^{-2}$ for the Gulf Stream) (Figs. 6a–f), were associated with cyclones located northeastward of the LSHF anomalies. At 1800 UTC 3 January 2008 (Figs. 6a–c) a strong LSHF was associated with a δT exceeding 15°C, δE exceeding $18\,g\,kg^{-1}$, and with the north winds exceeding $18\,m\,s^{-1}$. These conditions were formed by the interaction of the North American high (Harman 1987; Ioannidou and Yau 2008) with the cyclone propagating in the western North Atlantic. The North American high was located over the eastern part of the North America and was characterized by central pressure of 1040 hPa in the area south of Great Lakes. The associated strong SLP gradient [2.5–3 hPa $(100\,km)^{-1}$] implies cold air outbreak conditions with the southward advection of extremely dry and cold air over the warm Gulf Stream.

At 1800 UTC 22 January 2008 (Figs. 6d–f) the cold air outbreak conditions were primarily associated with the rear part of an intense cyclone over the Irminger Sea and the North American high displaced to the western midlatitude North Atlantic with SLP maximum in the center of 1035 hPa. A strong SLP gradient, exceeding 3 hPa $(100\,km)^{-1}$, resulted in northeasterly winds exceeding $25\,m\,s^{-1}$, which caused the advection of cold and dry air masses, resulting in a $\delta T > 15$°C and a LSHF greater than $1000\,W\,m^{-2}$.

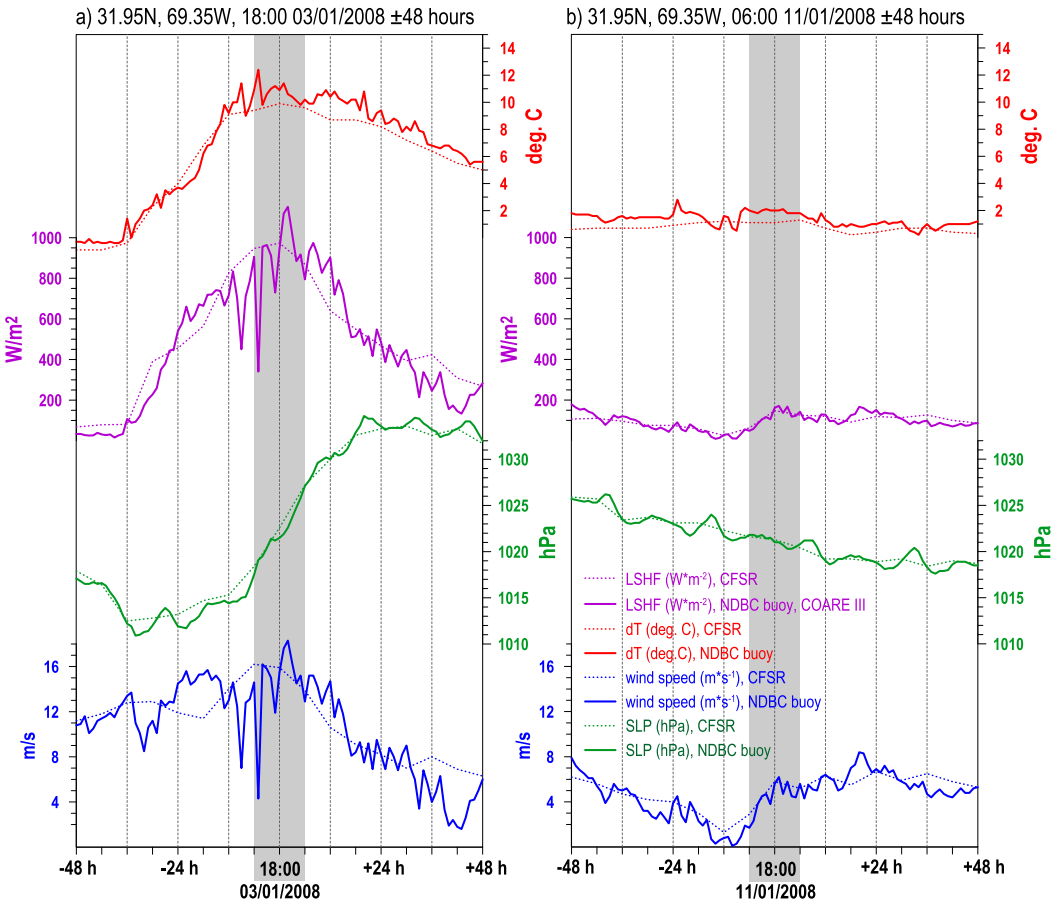

FIG. 7. Time series of the surface layer parameters in the location of NDBC buoy 41048 (31.95°N, 69.35°W) at (a) 1800 UTC 3 Jan 2008 ± 48 h and (b) 0600 UTC 11 Jan 2008 ± 48 h for LSHF (purple), SLP (green), δT (red), and scalar wind speed (blue). Bold lines stay for in situ measured parameters by NDBC buoy 41048 and computed fluxes, dotted lines stay for the collocated data from NCEP CFSR.

Figures 6g–i (0600 UTC 11 January 2008) show an alternative situation, which demonstrates that not all of the cyclones over the North Atlantic lead to very strong heat fluxes. Here, an intense cyclone over the western North Atlantic was associated with a negative LSHF anomaly of $-200\,\mathrm{W\,m^{-2}}$ (equivalent to LSHF of $100\,\mathrm{W\,m^{-2}}$, which is nearly 5 times smaller than the January mean). This situation was characterized by the absence of a strong high pressure system following the cyclone. Accordingly, the North American high was suppressed and the conditions over the western North America were characterized by the cyclone with a central pressure of 995 hPa located south of the Great Lakes, resulting in the northward advection of warm tropical air over the Gulf Stream with δT of 0°–3°C and moderate winds of $3–6\,\mathrm{m\,s^{-1}}$.

Figure 7a shows the temporal evolution of the conditions presented in Figs. 6a–c and Figs. 6g–i as revealed by NDBC buoy 41048 (31.95°N, 69.35°W) data (Meindl and Hamilton 1992). The LSHF values from the buoy data were calculated using the COARE-3 bulk algorithm (Fairall et al. 2003), which provides the adjustment of the wind speed, temperature, and humidity to the standard 10-m height. The period of 1–5 January 2008 was characterized by an abruptly growing SLP in the rear of the cyclone, with the maximum tendency of $5.5\,\mathrm{hPa\,(6\,h)^{-1}}$ on 3 January 2008 when the peak values of LSHF ($990\,\mathrm{W\,m^{-2}}$), δT (13°C), and northerly wind speed ($15\,\mathrm{m\,s^{-1}}$) were observed. The cyclonic conditions on 11 January 2008 were associated with the low and moderate LSHF values (Fig. 7b). This period was dominated by the northeastward advection, with wind of approximately $8\,\mathrm{m\,s^{-1}}$, δT varying within 2°–3°C, and LSHF of $150\,\mathrm{W\,m^{-2}}$, which is half that of the climatological wintertime mean.

Figure 8a shows the point correlations of the SLP tendencies and LSHF of the Gulf Stream area averaged over all of the 32 Januaries from 1979 to 2010.

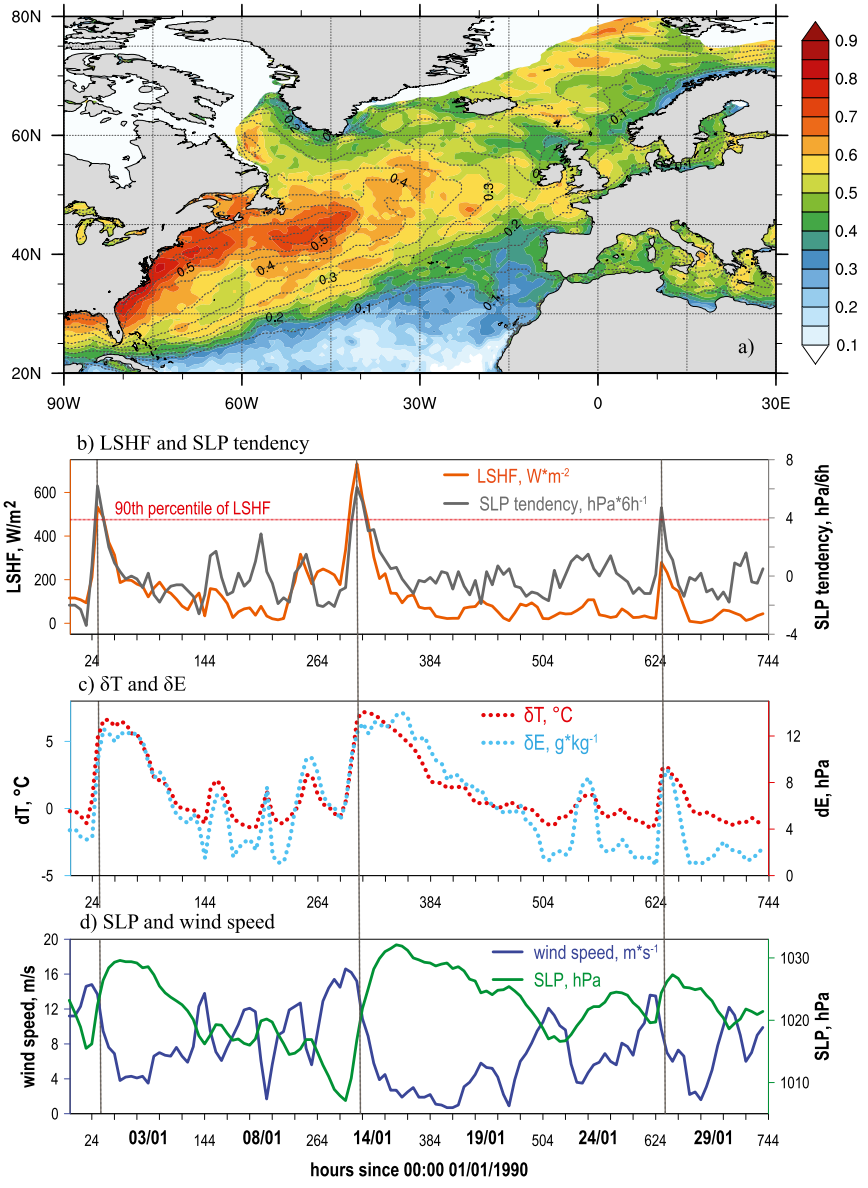

FIG. 8. (a) Averaged over Januaries from 1979 to 2010 (dotted contours) and maximum over the same period (colors) correlations between 6-hourly SLP tendencies [hPa $(6\,\mathrm{h})^{-1}$] and LSHF. (b)–(d) Time series of the surface layer parameters for the January 1990 in the location 31.95°N, 69.35°W from NCEP CFSR: (b) LSHF and SLP tendency, (c) δT and δE, and (d) SLP and wind speed.

The highest average correlation over the Gulf Stream is 0.75, with maximum correlations in individual years (also shown in Fig. 8a) as high as 0.9. This implies that the high LSHFs are closely associated with strong SLP gradients in the rear of the cyclone caused by the intense cold front and the high pressure system that follows the cold front. The presence of the cold front results in the cold air outbreak, which leads to intensification of the air–sea heat fluxes. The strength of cold air advection in the cold air outbreak (and the magnitude of the associated surface fluxes) can be to a large extent controlled by the strength of the large-scale pressure gradient associated with the high pressure system following the cyclone. The time series built from reanalysis (Figs. 8b–d) show that very strong LSHF events (14.01 and 28.01) are concurrent with the strongest SLP tendencies [6 hPa $(6\,\mathrm{h})^{-1}$], highest winds ($16\,\mathrm{m\,s^{-1}}$), and highest humidity and temperature vertical difference (δT and δE, 7°C and $13\,\mathrm{g\,kg^{-1}}$ respectively), while moderately high and low LSHFs were not associated with strong SLP tendencies.

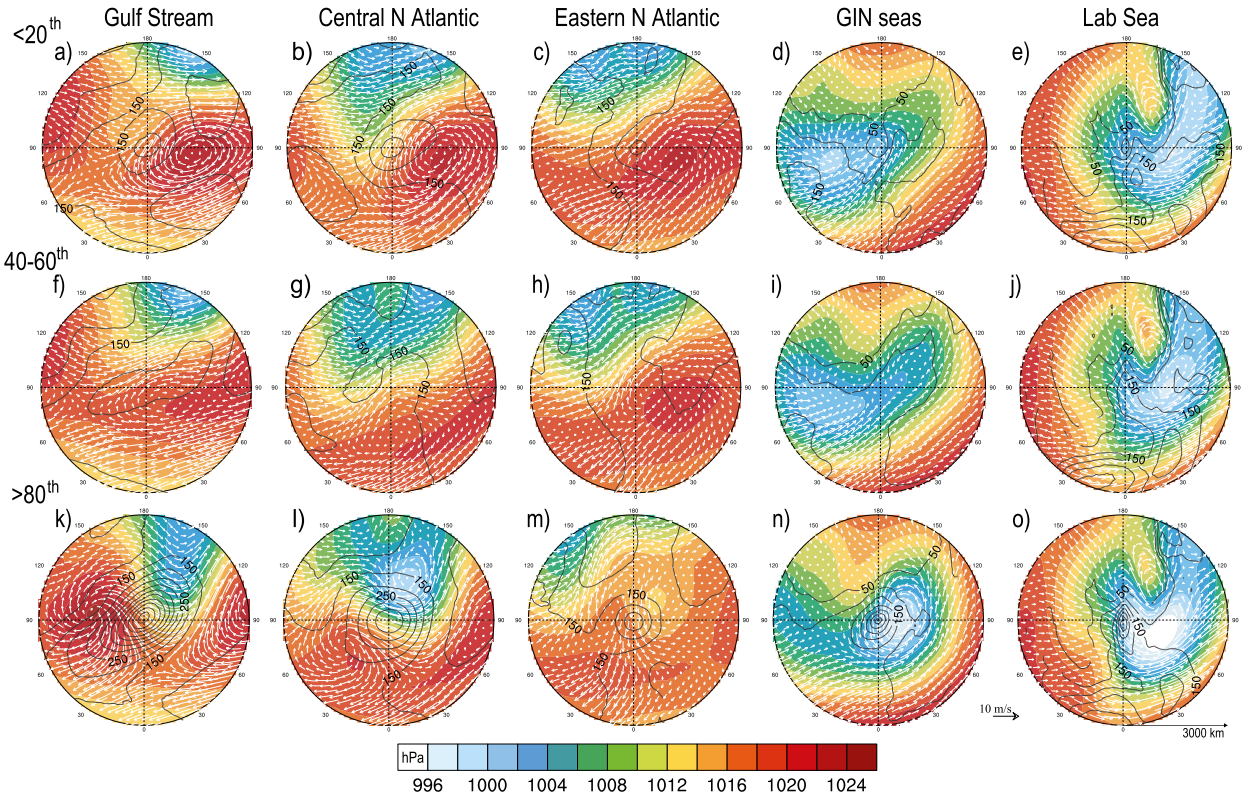

FIG. 9. Composites of SLP (hPa, color), LSHF ($W\,m^{-2}$, gray dotted contours), and 10-m wind (white vectors) for the three ranges of LSHF percentiles: (a)–(e) >20th percentile (''weak'' LSHF), (f)–(j) 40th to 60th percentiles (''moderate'' LSHF), and (k)–(o) >80th percentile (''strong to extreme'' LSHF). Columns are for different regions: (a),(f),(k) Gulf Stream; (b),(g),(l) central North Atlantic; (c),(h),(m) eastern North Atlantic; (d),(i),(n) GIN Seas; and (e),(j),(o) Labrador Sea. The number of events participating in the averaging is shown in Table 1, regionalization refers to Fig. 2a. Distributions of LSHF are masked in the areas where more than 80% of grid points fall to the land regions.

Thus, intense cyclones over the North Atlantic midlatitudes may result in both strong and weak surface turbulent heat fluxes. In cases when a cyclone is followed by a trailing anticyclone, an interaction zone is formed with strong SLP gradients and the advection of cold air from the north; thus leading to very strong and extreme values of surface fluxes. Alternatively, several cyclones clustered in a series form an active storm track but do not typically provide favorable conditions for high LSHF. In summary, our results suggest that the presence of a high pressure system following a cyclone is critically important for the formation of very strong and extreme surface turbulent fluxes.

b. *Composite analysis of atmospheric circulation conditions associated with LSHFs of different intensities*

Composites of atmospheric parameters were computed for heat flux events of different magnitude (weak, moderate, and strong) over the five regions in the North Atlantic (Fig. 2a) (see section 2c). Overall, between 1507 and 3270 cases (out of about 4000 cases composing the January 1979–2010 6-hourly data) (see TOT in Table 1) were used to build the composites in different regions (Figs. 9, 10). For the composites over the ocean (SST, δT, δE, LSHF) we masked out the areas of composites consisting of more than 80% of land points (see Fig. 2 and section 2c).

For the weak flux composites (<20th percentile, Figs. 9a–e and 10a–e), the LSHF patterns are characterized by minima in the composite center with the values ranging from $\sim 100\,W\,m^{-2}$ in the Labrador Sea and GIN Seas areas to $\sim 200\,W\,m^{-2}$ over the Gulf Stream. The corresponding SLP patterns over the Gulf Stream, central North Atlantic, and eastern North Atlantic regions are characterized by SLP maxima southeast of the composite center, implying relatively calm southerly winds ($2–6\,m\,s^{-1}$) that result in the northward advection of the warm air, providing weak surface temperature and humidity vertical difference (1°–2°C and $5–6\,g\,kg^{-1}$, respectively). The composites in the Labrador Sea and the GIN Seas regions are

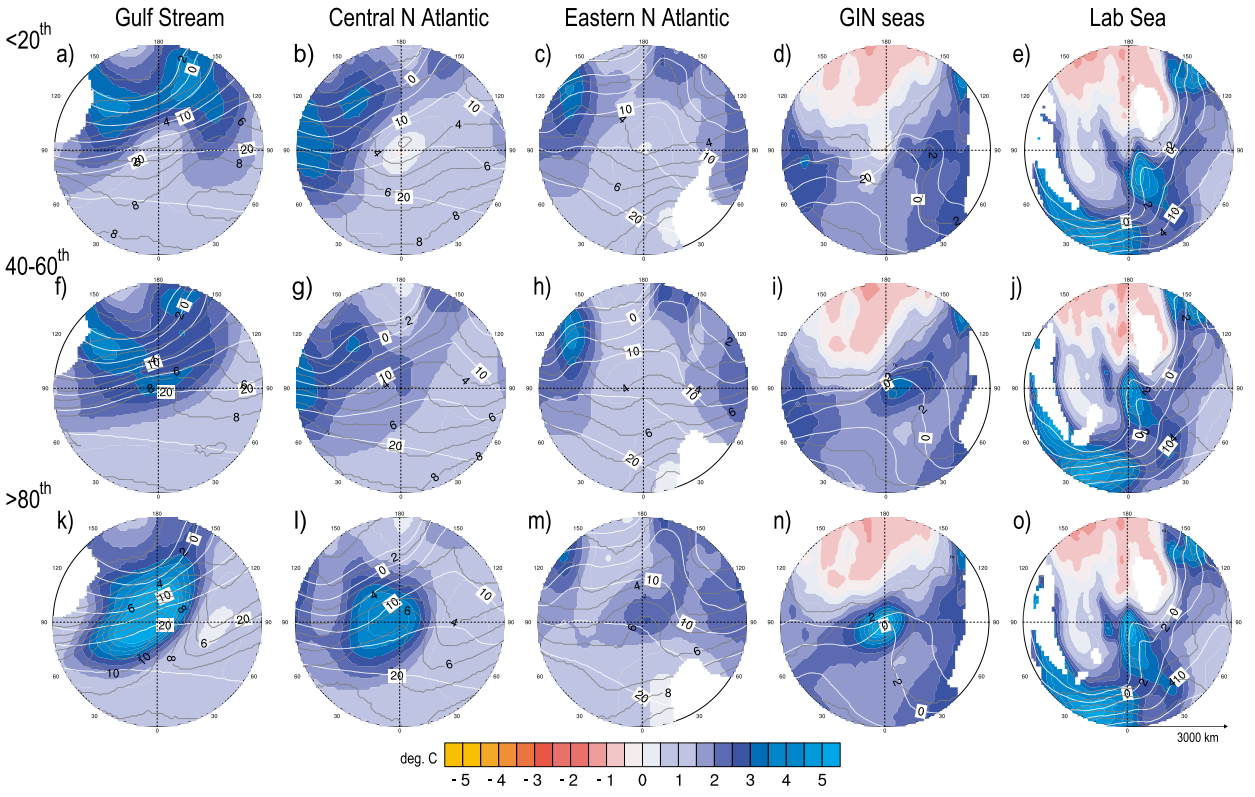

FIG. 10. Composites of the vertical temperature difference δT (SST minus 2-m air temperature, color, degrees), vertical humidity difference δE (computed saturation humidity at SST minus 2-m specific humidity, black lines, g kg^{-1}), and sea surface temperature (white contours, °C) for the three ranges of LSHF percentiles: (a)–(e) >20th percentile (''weak'' LSHF), (f)–(j) 40th to 60th (''moderate'' LSHF), and (k)–(o) >80th (''strong to extreme'' LSHF). Columns are for different regions: (a),(f),(k) Gulf Stream; (b),(g),(l) central North Atlantic; (c),(h),(m) eastern North Atlantic; (d),(i),(n) GIN Seas; and (e),(j),(o) Labrador Sea. The numbers of events participating in the averaging are shown in Table 1, and regionalization refers to Fig. 2a. Areas where more than 80% of grid points fall to the land regions are masked out.

characterized by low pressure systems located eastward (for the GIN Seas) and slightly northwestward (for the Labrador Sea) of the center of the LSHF composite. In both cases, the advection results in a decrease of the LSHF.

For the moderate heat fluxes (40th to 60th percentiles, Figs. 9f–j and 10f–j), the LSHF in the composite center exhibits values from ~125 W m^{-2} in the GIN Seas to the values greater than 250 W m^{-2} over the Gulf Stream. In the Gulf Stream, central North Atlantic, and eastern North Atlantic regions, a low-gradient high pressure field is causing variable advection. Over the GIN Seas and the Labrador Sea, the composites are dominated by a low pressure system, similar to the one in Figs. 9d and 9e. Over the GIN Seas, the low pressure system implies a northeastward advection that results in weak to moderate vertical temperature difference and LSHFs close to the climatological values. In the Labrador Sea, however, the composite of the atmospheric variables associated with moderate surface heat fluxes is similar to that for the situation with high LSHF (Figs. 9j,o), with winds exceeding 7–8 m s^{-1} and a southward advection leading to potentially high fluxes. Note that in the cold environments of the Labrador Sea and the GIN Seas, the regional statistics of the LSHF are largely dominated by the sensible fluxes that may introduce a bit of uncertainty in the attribution of the composites to the moderate fluxes.

The composites for the strong fluxes exceeding the 80th percentile (Figs. 9k–o and 10k–o) are characterized by the strongly localized maxima of the LSHF, with magnitudes ranging from 250 to more than 600 W m^{-2}. In all regions, the composites of the corresponding atmospheric conditions are characterized by the dipole consisting of the low pressure system northeastward and the high pressure system southwestward of the composite center. This structure implies strong northwesterly winds forming cold air outbreaks in the cyclone–anticyclone interaction zone where the δT and δE amount to 7°–10°C and 10–12 g kg^{-1}, respectively

(Figs. 10k–o). This structure is very robust over the Gulf Stream and central North Atlantic, but is somewhat less pronounced over the eastern North Atlantic where advection can be associated with both northwesterly (as in Figs. 9e and 9f) and northeasterly winds. Over the GIN Seas and the Labrador Sea, cold air outbreaks may also occur because of advection of the air over ocean from Greenland and Canadian Archipelago (Moore et al. 2014; Papritz 2017; Papritz and Spengler 2017). For example, the average wind speed over the Labrador Sea in the composite center amounts to 10–12 m s^{-1}, with a maximum exceeding 20 m s^{-1}.

The variability in the LSHFs heat fluxes (e.g., the formation of strong or weak heat fluxes) is dominated by the highly variable atmospheric parameters (SLP, wind, δT, and δE) and LSHFs, while the SST is quite stable and close to its climatological values (Fig. 10). This illustrates the leading role of the atmosphere in the LSHF variability at the synoptic time scale and explains variable cold airmass availability (Iwasaki et al. 2014; Shoji et al. 2014) in the set of composites of Fig. 10.

c. *Independence of composite members and robustness of composites of atmospheric circulation conditions*

Composites in Figs. 9 and 10 were computed from the entire sample of the corresponding heat flux events, including the events of very short duration and the events that are potentially interdependent. To investigate the impact of short-lived LSHF events on our analysis, we also performed composite analysis using only the events lasting longer than 18 h (TOT18 in Table 1). The number of these events is 30%–50% as small as the total number of the events considered (Fig. 3 and Table 1). Examples of composites built from this reduced sample for the Gulf Stream and Labrador Sea and for LSHF > 80th percentile of its CDF are shown in Figs. 11a and 11b. (The full set of composites is presented in supplemental Fig. S2.) Figures 11a and 11b (and supplemental Fig. S2) show that these composites are consistent with the composites built from the whole sample (TOT in Table 1) and the differences between the composites are not statistically significant according to the Student's t test (see supplemental Fig. S3).

Finally, in order to account for the effect of serially dependent LSHF events originating from passing cyclones, we analyzed composites built from only the first and the last time moments of LSHF anomalies lasting longer than 18 h. The number of these composite members (IND18 in Table 1) is always less than 100, which is more than 10 times smaller compared to the total number of events. Composites built from these reduced ensembles for the percentile range corresponding

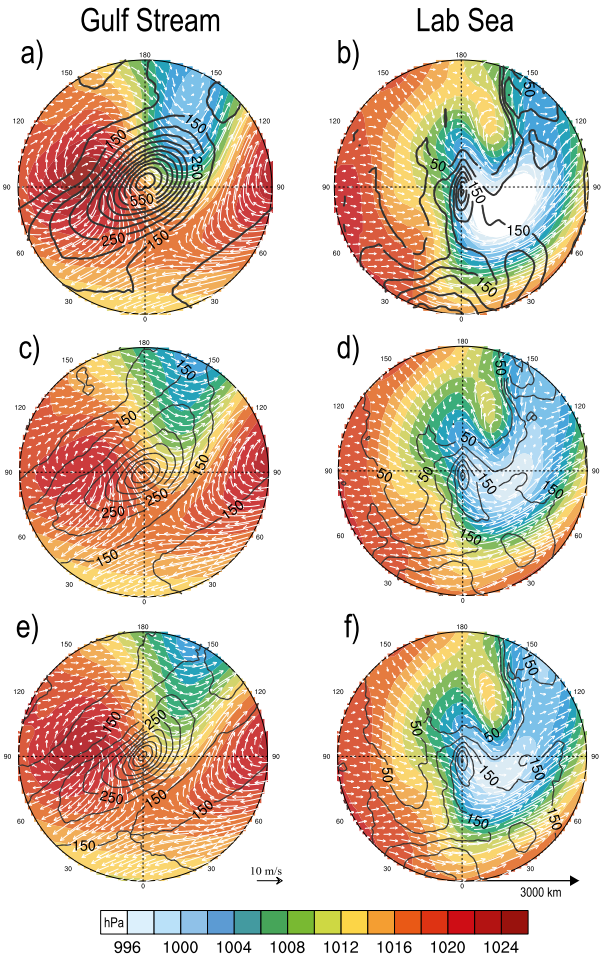

FIG. 11. (a),(b) Composites of SLP (hPa, color), LSHF (W m^{-2}, black lines), and 10-m wind (m s^{-1}, white vectors) for the ranges of strong LSHF (>80th percentile) in (a) Gulf Stream and (b) Labrador Sea. These composites are built from the reduced samples of all 6-hourly snapshots for the events lasting longer than 18 h (TOT18 in Table 1). (c)–(f) The same composites built from only the (c),(d) first and (e),(f) last time steps of LSHF anomaly lasting longer than 18 h (IND18 in Table 1) in the (c),(e) Gulf Stream and (d),(f) Labrador Sea.

to strong fluxes (>80th percentile) (Figs. 11c–f) only show minor differences with respect to one another; these differences are not statistically significant. Qualitatively, the composites in Figs. 11c–e are also very similar to those presented in Fig. 9 (and supplemental Fig. S2). At the same time, compared to the composites shown in Fig. 9 and Figs. 11a and 11b, these composites do demonstrate somewhat smaller LSHFs and smaller SLP gradients and winds, which is quite reasonable for the initial and the decaying stages of the events considered. Thus, our results are robust with respect to the selection of composite members. Furthermore, the analysis of differences in surface fluxes and surface state variables for all of the composites (not shown)

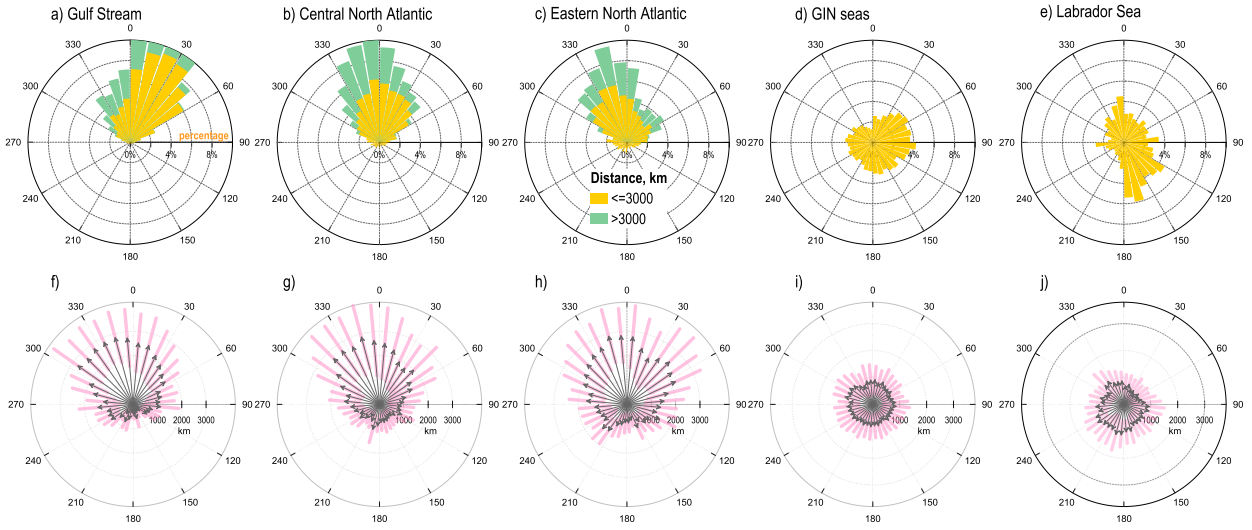

FIG. 12. (a)–(e) Directional distribution (roses, %) of the locations of the nearest cyclone centers with respect to the ''mass centers'' of the LSHF exceeding the 50th percentile for the five regions over the North Atlantic (see Fig. 2a) for Januaries 1979–2010. Yellow and green petals show the percentages of cyclones located within the 3000-km radii and outside the 3000-km radii. (f)–(j) Directional distributions of the averaged distances between the nearest cyclone centers and the mass centers for the LSHF exceeding the 50th percentile (gray vectors) along with ±1 standard deviation error bars of distanced (pink bars).

demonstrated that the differences between the composites associated with weak, moderate, and strong fluxes are statistically significant at the 5% level according to the Student's *t* test (except for the differences associated with moderate and strong heat flux cases in the Labrador Sea).

To summarize, the composite analysis clearly shows that the very strong LSHFs over the North Atlantic are typically associated with the cyclone–anticyclone interactions zones, which are characterized by strong pressure gradients and strong winds in a primarily southward direction. Thus, an anticyclone following the cyclone is a critical feature in formation of surface heat flux extremes over the entire midlatitude North Atlantic.

5. Linking ocean turbulent heat fluxes to the characteristics of cyclonic activity

To relate magnitudes of LSHFs with cyclones over the North Atlantic, we analyzed the cyclone tracks associated with the LSHF events of different intensity. On the interannual time scales, the surface turbulent fluxes are well correlated with the North Atlantic Oscillation (NAO) index (Cayan 1992a,b; Iwasaka and Wallace 1995; Visbeck et al. 2003; Tanimoto et al. 2003; Gulev et al. 2007 among many others). The pronounced correlation of the cyclone activity with the NAO index has been reported in numerous studies (Gulev et al. 2001, 2002; Jung et al. 2003; Pinto et al. 2009). However, the robust links between the variability of the cyclone characteristics and surface turbulent heat fluxes have not yet been found. Correlations between heat flux magnitudes and the characteristics of cyclone activity do not exceed 0.5, even in winter (not shown). This reflects the specific nature of the very strong and extreme LSHF events, which, as shown above, are associated with the cyclones followed by the high pressure systems.

We associated the local atmospheric conditions resulting in LSHF events of different intensities with cyclones even if these cyclones were quite remote from the center of the analyzed LSHF event. For this purpose, we searched, at each 6-hourly time step, for the cyclone closest to the center of mass of the LSHF area considered. The directional distributions of the locations of such cyclone centers for the LSHF with the magnitudes exceeding the 50th percentile of the LSHF distribution are shown in Fig. 12. For the Gulf Stream and central North Atlantic regions, the most likely cyclone candidates are located northeastward and northward of the LSHF anomaly, consistent with Fig. 9. For the eastern North Atlantic region, the associated cyclone centers are located northwestward, also in agreement with Fig. 9. In the GIN Seas, the cyclones associated with the strong LSHFs are homogeneously distributed around the flux anomaly, implying that the cold air outbreak conditions could be provided by variable advection in addition to the cold airmass falls near Greenland. In the Labrador Sea, there are two preferred sectors of cyclones associated with the high LSHFs: the regions north

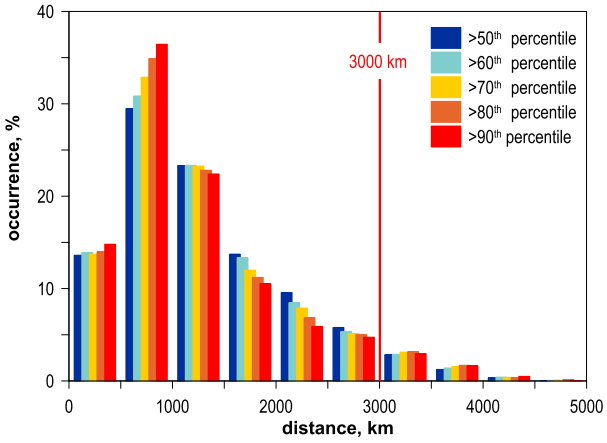

FIG. 13. Probability distributions of distances between the "mass centers" of LSHF areas exceeding different percentiles and the nearest cyclone centers over the North Atlantic (north of 25°N) for Januaries during the 1979–2010 period.

of the high LSHF areas (advection from the Canadian Archipelago) and those southward (advection from Greenland).

Figure 13 shows the probability distributions of the distances between the centers of mass of the areas corresponding to LSHF events associated with the magnitudes exceeding the 50th to 90th percentile thresholds of the LSHF's CDF, as well as the corresponding cyclone centers over the entire North Atlantic. Remarkably, the shape of the distribution is quite robust with respect to the percentile threshold used, with the modal values ranging from 500 to 1500 km and more than 85% of the associated cyclones falling within a radius of 3000 km from the location of extreme LSHF. The average cyclone radius is 400–600 km in the Labrador Sea and GIN Seas and is around 800 km over the entire midlatitude region (Rudeva and Gulev 2007). Regional directional distributions of the locations of the cyclone centers associated with the high LSHF values for the search distances less than and greater than 3000 km (Fig. 12) are qualitatively consistent with one another in all regions. Thus, the 3000-km distance derived from Fig. 13 can be considered a reasonable threshold for association of the LSHF anomalies with individual cyclones.

Figure 14a shows the fraction of cyclone tracks (with respect to the total count over the North Atlantic) associated with the LSHFs exceeding different percentiles of the LSHF CDF (from the 50th to the 99th). Note that the LSHF events are frequently associated with cyclones located outside of the five regions analyzed in this study. For instance, a strong flux in the Gulf Stream area can be caused by a large cyclone whose center is located over continental North America or rather east of the Gulf Stream area over the central North Atlantic. For this reason, in Fig. 14, we analyze all the cyclone tracks identified within 3000 km of the 5 regions, as implied by Fig. 13. We considered a cyclone to be associated with an LSHF anomaly if it approached the area of a given heat flux anomaly at least once during its life cycle. For 1979–2010, the LSHF events exceeding the 50th percentile of the LSHF distribution turned out to be associated with approximately 50% of the cyclone trajectories over the North Atlantic. The relative numbers of cyclones associated with all of the moderate-to-strong LSHF events peaked when the distance between the cyclone center and the location of each LSHF event was 1500 km (Fig. 14a).

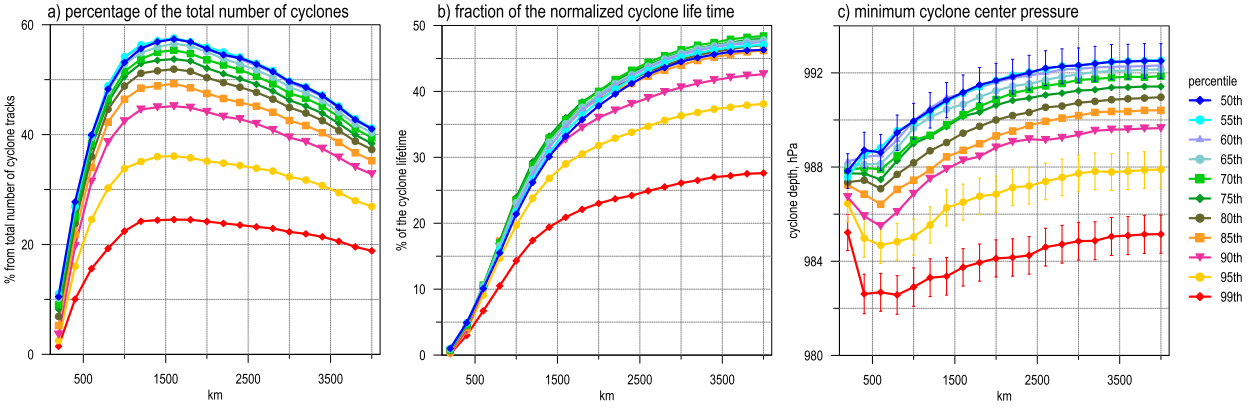

FIG. 14. (a) Percentage of cyclone tracks over the North Atlantic associated with LSHF events of different percentiles as a function of the threshold distance between the LSHF area "mass center" and the cyclone center. The total sample of cyclones for every threshold consisted of all cyclone tracks north of 25°N. (b) Fraction of cyclone lifetime (%) during which the cyclone is associated with LSHF of different percentiles. (c) Minimum cyclone central pressure, as a function of the threshold distance between LSHF area mass center of different percentile and the associated cyclone center.

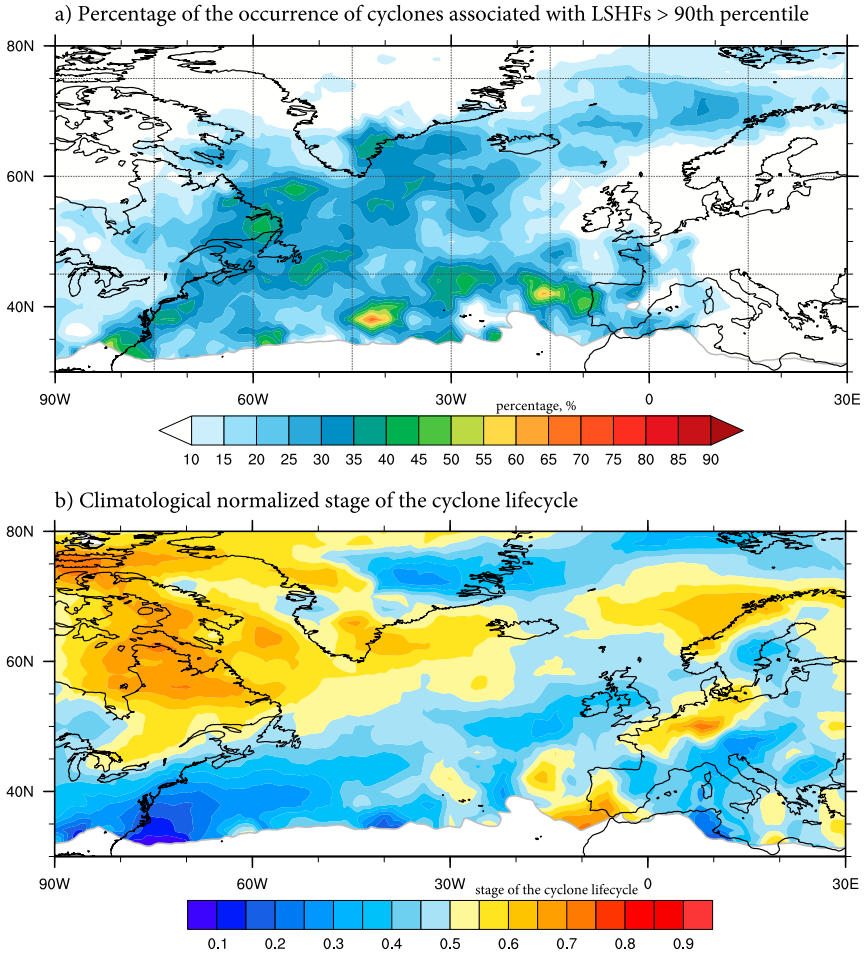

FIG. 15. (a) Spatial distribution of the percentage (%) of the occurrence of the centers of cyclones associated with LSHF events exceeding the 90th percentile and falling into the 3000-km radii search area. (b) Climatological normalized stage of the cyclone life cycle (from 0 to 1) over the North Atlantic in January for the period of 1979–2010. Bold gray line indicates the area (was masked) with a rare cyclone occurrence of less than 1 cyclone per 155 000 km^2.

Importantly, very strong LSHF episodes may occur over a short period during the cyclone life cycle. In Fig. 14b, we show the durations (normalized by the cyclone lifetime) of the association of the cyclones with the LSHF anomalies. The duration of the cyclone association with strong and very strong flux events is shorter than that with the moderate flux events (e.g., 20% of the lifetime for the 99th percentile vs 35% for the 50th percentile). Figure 14c shows that on average, the cyclones associated with the strong fluxes are clearly deeper compared to the others. For example, for the 99th percentile of LSHF values, the central pressure of the cyclones associated with the LSHF events exceeding the 99th percentile of the LSHF distribution decreases by approximately 8 hPa compared to that of the cyclones associated with the >50% LSHF events.

The combined effect of the number of the storm tracks (Fig. 14a) and the fraction of the cyclone lifetimes (Fig. 14b) on the occurrence of cyclone association with strong LSHFs is illustrated in Fig. 15a, which shows the ratio between the frequency of cyclones associated with LSHFs exceeding the 90th percentile of the LSHF CDF and the total cyclone frequency. Over the main North Atlantic storm track, 10%–50% of cyclone events are associated with LSHF values exceeding the 90th percentile. The maximum frequency of these events is identified over the North American coast, in the Labrador Sea and GIN Seas. The higher fractions (up to 70%) found in the eastern North Atlantic should be treated with caution, as the number of cyclones there is small compared to that over the major storm track.

Figure 15b shows the January climatology of the normalized cyclone age for all cyclones over the North

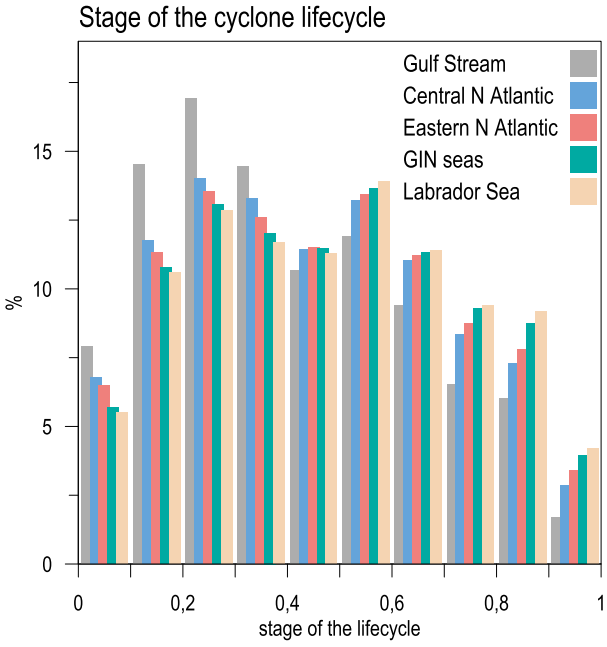

FIG. 16. Probability distributions of the normalized stage of cyclone life cycle on which cyclones are associated with very strong LSHF events exceeding the 90th percentile and falling into the 3000-km radii search area for different regions. Regionalization refers back to Fig. 2a.

Atlantic. It implies that over the Labrador Sea and GIN Seas cyclones are in the mature stage of their development, while over the main storm track, cyclones are younger, with the youngest cyclones found over the Gulf Stream area. Figure 16 shows the histograms of the age of cyclones associated with the strong LSHF events. Over the Gulf Stream, the cyclones are typically associated with strong LSHF events during early stages of their development, with normalized cyclone age within the 0.1–0.3 (equivalent to the range from a few hours to 1–3 days). In the central North Atlantic and eastern North Atlantic, the cyclones cause very strong LSHFs at both initial development and mature stages (0.3–0.7), which is 0.1–0.2 lifetime units longer than that for all cyclones. In the GIN Seas and Labrador Sea, strong fluxes are primarily associated with more mature stages of cyclone development.

The overall assessment is that over the cyclogenesis areas (Gulf Stream, GIN Seas, and partly east of Greenland), cyclones tend to cause strong LSHF events at the stage of initial cyclone development after the generation. Over the rest of the North Atlantic, cyclones tend to cause flux extremes at more mature stages. Note, however, that the large-scale advection of the cold air could be the result of a more mature cyclone farther away. It is also possible that some cyclones associated with the strong heat flux events are secondary cyclones that develop in the preexisting frontal zone. One might argue about the accuracy of identification of cyclone generation moment by the tracking algorithm. However, we consider here the first 20% of the cyclone lifetime (normalized age 0–0.2). At this stage cyclones exhibit conditions of strong baroclinicity implying rapid intensification and strong wind speeds (Schemm et al. 2015; Kuwano-Yoshida and Asuma 2008; Kuwano-Yoshida and Enomoto 2013). Moreover, our tracking scheme is based on SLP and, thus, potentially tends to identify cyclones a bit later than vorticity-based schemes (Hodges et al. 2003; Neu et al. 2013; Rudeva et al. 2014).

Figure 17 quantifies the cyclone life cycle characteristics (central pressure, deepening rate, and propagation velocity) for the cyclones associated with LSHF events

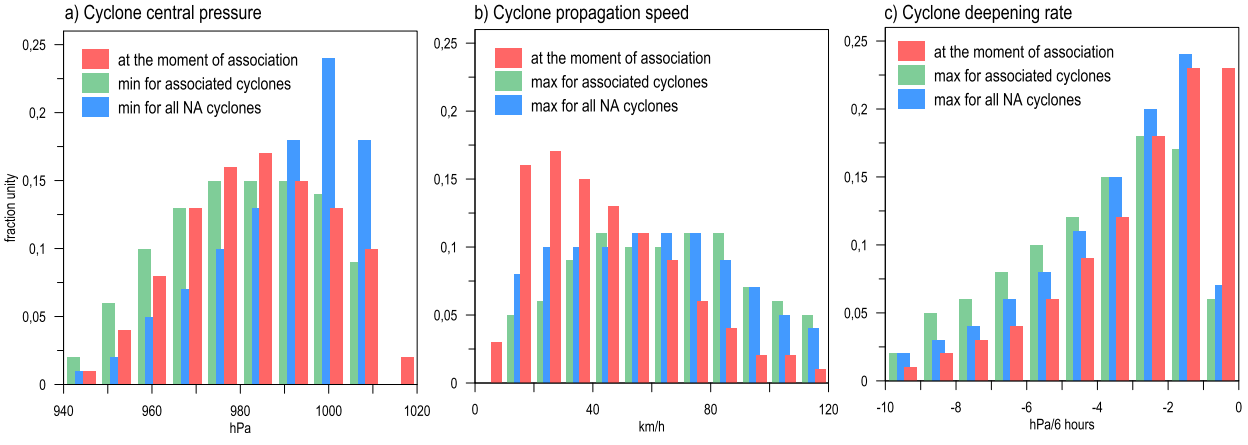

FIG. 17. Probability distributions of the cyclone (a) minimum central pressure, (b) maximum cyclone propagation speed, and (c) maximum cyclone deepening rate for all cyclones over the North Atlantic (blue), cyclones associated with LSHF events exceeding the 90th percentile (green), and at the moments of the cyclone life cycle (cyclone trajectory steps) when cyclones were associated with LSHF events exceeding the 90th percentile (pink).

exceeding the 90th percentile of the LSHF distribution and those for the whole North Atlantic (not conditioned on the LSHF events). Approximately 35% of the cyclones associated with strong fluxes are deeper than 970 hPa, although this is the case for only about 20% of all cyclones (Fig. 17a). While the cyclone propagation velocities of the two subsets are similar (Fig. 17b), the cyclones associated with strong LSHF events also exhibited greater deepening than all cyclones (Fig. 17c). Note that Sanders and Gyakum (1980) used daily deepening rates for identifying rapidly intensifying cyclones. Here we analyzed 6-hourly deepening rates to keep consistency with LSHF events (also analyzed for 6-hourly time steps). Figure 17c shows that the occurrence of cyclones with maximum deepening rates greater than 6 hPa $(6\,\mathrm{h})^{-1}$ is 15% higher in the subset of cyclones associated with strong LSHF. Histograms of the life cycle characteristics for the periods of the association of cyclones with strong LSHF events demonstrate that on average, and over the whole North Atlantic, this association tends to occur for the cyclones with smaller propagation velocities and lower deepening rates. This can be explained by the dominance of cyclones in the central North Atlantic, eastern North Atlantic, and Labrador Sea regions over the Gulf Stream cyclones in the total sample (Table 1). In the former regions, the association of cyclones with strong LSHF events occurs at the mature stage of cyclone development (Fig. 15).

6. Summary and discussion

We analyzed the atmospheric drivers behind the formation of LSHFs of different intensities in the midlatitudes of the North Atlantic and investigated the role of midlatitude cyclones in the formation of strong and extreme surface flux events in winter. Strong LSHFs with magnitudes exceeding 80th percentile of the LSHF distribution, significantly contributing to the total area-integrated LSHF, are found to be primarily associated with the cyclone–anticyclone interaction zones. These zones provide the preconditions for the cold air outbreaks characterized by the extremely high air–sea temperature and humidity differences and strong winds. In this respect, the active North Atlantic storm track with serial cyclone clustering is less favorable for the occurrence of very strong LSHF events than a cyclone followed by an anticyclone forming an interaction zone. Over the western and central North Atlantic, the latter conditions are closely associated with the North American high interaction with propagating or blocked cyclones, leading to the formation of cold air outbreaks. Regional composites of the surface state variables conditioned on the magnitude of LSHFs clearly demonstrate that for the strong LSHF events in the North Atlantic region, the atmospheric conditions are characterized by the dipoles of low pressure system northeastward and the high pressure system southwestward of the LSHF local maximum, collocated with strong winds and very high vertical temperature and humidity differences. Further analysis of cyclone tracks associated with the LSHF events of different magnitudes demonstrated that cyclones responsible for the very high fluxes are considerably deeper than average and more frequently experience rapid intensification. These cyclones constitute approximately 20%–40% of all North Atlantic cyclones and generate favorable conditions for strong LSHF events during short periods amounting to 15%–20% of their lifetimes; specifically, at the earlier stage of the life cycle in the regions of cyclogenesis and at more mature stages over the rest of the North Atlantic.

Our analysis shows that the intense air–sea flux events in the North Atlantic are not associated with the intensification of the North Atlantic storm track, but rather with cyclones interacting with anticyclones. Many of these cyclones occur during blocking conditions over the North Atlantic (as shown in Fig. 6). For instance, Booth et al. (2017) demonstrated that mid-Atlantic blocking may result in intensification of cyclones over the Gulf Stream. In this respect, reanalyzing the blocking activity over the North Atlantic (Wiedenmann et al. 2002; Barriopedro et al. 2006) and its alternation with periods of intense serial cyclone clustering (Mailier et al. 2006; Pinto et al. 2013) is of great interest.

Another important issue for understanding the large-scale mechanisms driving the occurrences of very strong and extreme LSHFs is the long-term evolution of the North American high. The North American high was first investigated in the pioneering diagnostic works by Reed (1933, 1937) who pointed to its origination from the upper-level ridges mostly in the western part of North America. Zishka and Smith (1980) analyzed the 27-yr climatology and demonstrated a robust wintertime pattern of the near-surface anticyclone frequencies over eastern North America, with anticyclone central pressure typically exceeding 1020 hPa.

The formation of the North American high is primarily associated with adiabatic vorticity and the thermal advection originating from Alaska (Tan and Curry 1993; King et al. 1995). Lupo et al. (1992) demonstrated that rapid intensification of the western North Atlantic cyclones occurs in conjunction with a well-developed North American high pattern. Several studies reported that, while the North American high is quite persistent, it can experience migrations over the eastern North America (e.g., Ellis et al. 2018). Harman (1987) has

shown that the continental anticyclone associated with the North American high can frequently extend to the western North Atlantic, which might play an important role in creating favorable conditions for the formation of strong LSHF, as demonstrated in Fig. 9. This is also demonstrated by Catalano and Broccoli (2018) in their analysis of cyclone activity along the northeastern U.S. coast and by Nieto Ferreira and Hall (2015), who analyzed surface temperature patterns associated with the North American high–North Atlantic gradients.

In this regard, the long-term reconstruction of the magnitude of the North American high is very important for further diagnosing its role in the formation of cold air outbreaks and strong air–sea heat fluxes, as the surface pressure gradients between cyclones and the North American high depend on both the cyclone depth and the North American high's central pressure. Also important is the analysis of the driving mechanisms of the North American high, which may help associate the multiyear time series of LSHFs over the North Atlantic with the North American high behavior. This association may have important implications for a possible connection between the magnitude of the North American high and the associated strong LSHFs over the North Atlantic with large-scale circulation modes over the NH, specifically within the Pacific [i.e., the Pacific–North American pattern (PNA) and Arctic Oscillation (AO)]. Recently, Dai and Tan (2017) demonstrated that different stages of the AO have a pronounced connection with the North American high. Another quasi-stationary high pressure system that may play a similar role to the North American high and affect the formation of the strong air–sea fluxes in the Labrador Sea and GIN Seas regions is the Beaufort Sea high (Serreze and Barrett 2011).

Very strong LSHFs, exceeding the 90th percentile of LSHF distribution, which are largely formed by synoptic conditions and are associated with approximately 30%–45% of all North Atlantic cyclones for 20%–25% of their lifetime (Figs. 13–16), may have an integrated feedback effect on the characteristics of cyclone activity over the North Atlantic, including impacts on the continental climate. Diagnostic studies (e.g., Gulev et al. 2002; Zolina and Gulev 2003; Parfitt and Czaja 2016; Woollings et al. 2016) suggest that SST gradients and the corresponding heat flux anomalies over the Gulf Stream affect baroclinic wave activity in the atmosphere. However, a diagnostic approach can hardly isolate the responses of atmospheric synoptic variability to the oceanic forcing from the impacts of this variability on surface fluxes. Quantification of the responses of storm tracks to the surface flux signal requires numerical modeling. Model results (Kuwano-Yoshida et al. 2010; Sasaki et al. 2012; Ma et al. 2015 a,b; Parfitt et al. 2016, 2017; O'Reilly et al. 2017) do demonstrate such a response. Kuwano-Yoshida and Minobe's (2017) modeling work demonstrated the association of cyclone deepening rates with the surface fluxes in the Kuroshio region consistent with our results (Fig. 16c). In this respect, further applications of the methods suggested here for the analysis of model experiments will be useful.

Further analysis of the association of extreme LSHF events with atmospheric synoptic and mesoscale variability requires high-resolution data of both the air–sea fluxes and the atmospheric variables. Surface flux products available from satellite data (Bentamy et al. 2017) and high-resolution modeling (Condron and Renfrew 2013; Moore et al. 2015) may help better locate very strong LSHF events and to quantify their association with atmospheric disturbances. On the atmospheric side, the inferred characteristics of cyclone activity and cyclone life cycle strongly depend on model and observational resolutions (Jung et al. 2006; Hodges et al. 2011; Tilinina et al. 2013, 2014). Higher-resolution regional reanalysis datasets (e.g., ASR; Wilson et al. 2012) and ERA-5 (Hersbach and Dee 2016) will help better quantify the mechanisms linking atmospheric synoptic and mesoscale dynamics with surface fluxes, especially in the subpolar regions. Moreover, such products, in conjunction with advanced diagnostic approaches (e.g., Papritz and Spengler 2015) will help quantify the association of surface fluxes with the mesoscale phenomena inside the cyclones, such as frontal systems (Schemm et al. 2015; Parfitt et al. 2017). In this respect, the analysis of precipitation and water recycling in the cyclones (Rudeva and Gulev 2011; Booth et al. 2018; Naud et al. 2018) is also of a great interest.

Acknowledgments. The NCEP CFSR output is available courtesy of the NOAA/National Weather Service/National Centers for Environmental Prediction. Analysis of cyclone activity (NT and AG) was supported by the Russian Science Foundation Grant 17-77-20112, and the analysis of surface fluxes (SKG) was supported by the project 14.W03.31.0006 funded by the Russian Ministry of Education and Science and by Russian Science Foundation Grant 14-17-00697. We thank Irina Rudeva of the University of Melbourne for the useful advice on the development of the compositing methodology, Marina Aleksandrova of IORAS for helpful insights, and Sergey Kravtsov of the University of Wisconsin–Milwaukee for useful comments on the paper text. We greatly appreciate extremely helpful and valuable comments of the two anonymous reviewers and Editor Dr. Ron McTaggart-Cowan, which helped to considerably improve the manuscript.

REFERENCES

Akima, H., 1970: A new method of interpolation and smooth curve fitting based on local procedures. *J. Assoc. Comput. Mach.*, **17**, 589–602, https://doi.org/10.1145/321607.321609.

Alexander, M. A., and J. D. Scott, 1997: Surface flux variability over the North Pacific and North Atlantic Oceans. *J. Climate*, **10**, 2963–2978, https://doi.org/10.1175/1520-0442(1997)010<2963:SFVOTN>2.0.CO;2.

Allen, J. T., A. B. Pezza, and M. T. Black, 2010: Explosive cyclogenesis: A global climatology comparing multiple reanalyses. *J. Climate*, **23**, 6468–6484, https://doi.org/10.1175/2010JCLI3437.1.

Barriopedro, D., R. García-Herrera, A. R. Lupo, and E. Hernández, 2006: A climatology of Northern Hemisphere blocking. *J. Climate*, **19**, 1042–1063, https://doi.org/10.1175/JCLI3678.1.

Bentamy, A., and Coauthors, 2017: Review and assessment of latent and sensible heat flux accuracy over the global oceans. *Remote Sens. Environ.*, **201**, 196–218, https://doi.org/10.1016/j.rse.2017.08.016.

Bishop, S. P., R. J. Small, F. O. Bryan, and R. A. Tomas, 2017: Scale dependence of midlatitude air–sea interaction. *J. Climate*, **30**, 8207–8221, https://doi.org/10.1175/JCLI-D-17-0159.1.

Bond, N. A., and M. F. Cronin, 2008: Regional weather patterns during anomalous air–sea fluxes at the Kuroshio Extension Observatory (KEO). *J. Climate*, **21**, 1680–1697, https://doi.org/10.1175/2007JCLI1797.1.

Booth, J. F., E. Dunn-Sigouin, and S. Pfahl, 2017: The relationship between extratropical cyclone steering and blocking along the North American East Coast. *Geophys. Res. Lett.*, **44**, 11 976–11 984, https://doi.org/10.1002/2017GL075941.

——, C. M. Naud, and J. Willison, 2018: Evaluation of extratropical cyclone precipitation in the North Atlantic Basin: An analysis of ERA-Interim, WRF, and two CMIP5 models. *J. Climate*, **31**, 2345–2360, https://doi.org/10.1175/JCLI-D-17-0308.1.

Bourassa, M. A., and Coauthors, 2013: High-latitude ocean and sea ice surface fluxes: Challenges for climate research. *Bull. Amer. Meteor. Soc.*, **94**, 403–423, https://doi.org/10.1175/BAMS-D-11-00244.1.

Brodeau, L., B. Barnier, S. K. Gulev, and C. Woods, 2017: Climatologically significant effects of some approximations in the bulk parameterizations of turbulent air–sea fluxes. *J. Phys. Oceanogr.*, **47**, 5–28, https://doi.org/10.1175/JPO-D-16-0169.1.

Catalano, A. J., and A. J. Broccoli, 2018: Synoptic characteristics of surge-producing extratropical cyclones along the northeast coast of the United States. *J. Appl. Meteor. Climatol.*, **57**, 171–184, https://doi.org/10.1175/JAMC-D-17-0123.1.

Cayan, D. R., 1992a: Variability of latent and sensible heat fluxes estimated using bulk formulae. *Atmos.–Ocean*, **30**, 1–42, https://doi.org/10.1080/07055900.1992.9649429.

——, 1992b: Latent and sensible heat flux anomalies over the northern oceans: The connection to monthly atmospheric circulation. *J. Climate*, **5**, 354–369, https://doi.org/10.1175/1520-0442(1992)005<0354:LASHFA>2.0.CO;2.

Chechin, D. G., C. Lüpkes, I. A. Repina, and V. M. Gryanik, 2013: Idealized dry quasi 2-D mesoscale simulations of cold-air outbreaks over the marginal sea ice zone with fine and coarse resolution. *J. Geophys. Res. Atmos.*, **118**, 8787–8813, https://doi.org/10.1002/jgrd.50679.

Clayson, C. A., and A. S. Bogdanoff, 2013: The effect of diurnal sea surface temperature warming on climatological air–sea fluxes. *J. Climate*, **26**, 2546–2556, https://doi.org/10.1175/JCLI-D-12-00062.1.

Condron, A., and I. A. Renfrew, 2013: The impact of polar mesoscale storms on northeast Atlantic Ocean circulation. *Nat. Geosci.*, **6**, 34–37, https://doi.org/10.1038/ngeo1661.

Dai, P., and B. Tan, 2017: The nature of the Arctic Oscillation and diversity of the extreme surface weather anomalies it generates. *J. Climate*, **30**, 5563–5584, https://doi.org/10.1175/JCLI-D-16-0467.1.

DuVivier, A. K., J. J. Cassano, A. Craig, J. Hamman, W. Maslowski, B. Nijssen, R. Osinski, and A. Roberts, 2016: Winter atmospheric buoyancy forcing and oceanic response during strong wind events around southeastern Greenland in the Regional Arctic System Model (RASM) for 1990–2010. *J. Climate*, **29**, 975–994, https://doi.org/10.1175/JCLI-D-15-0592.1.

Ellis, A. W., M. L. Marston, and D. A. Nelson, 2018: An air mass-derived cool season climatology of synoptically forced Appalachian cold-air damming. *Int. J. Climatol.*, **38**, 530–542, https://doi.org/10.1002/joc.5189.

Fairall, C. W., E. F. Bradley, J. E. Hare, A. A. Grachev, and J. B. Edson, 2003: Bulk parameterization of air–sea fluxes: Updates and verification for the COARE algorithm. *J. Climate*, **16**, 571–591, https://doi.org/10.1175/1520-0442(2003)016<0571:BPOASF>2.0.CO;2.

——, and Coauthors, 2011: Implementation of the Coupled Ocean-Atmosphere Response Experiment flux algorithm with CO_2, dimethyl sulfide, and O_3. *J. Geophys. Res. Oceans*, **116**, C00F09, https://doi.org/10.1029/2010JC006884.

Fleagle, R. G., N. A. Bond, and W. A. Nuss, 1988: Atmosphere-ocean interaction in mid-latitude storms. *Meteor. Atmos. Phys.*, **38**, 50–63, https://doi.org/10.1007/BF01029947.

Giordani, H., and G. Caniaux, 2001: Sensitivity of cyclogenesis to sea surface temperature in the northwestern Atlantic. *Mon. Wea. Rev.*, **129**, 1273–1295, https://doi.org/10.1175/1520-0493(2001)129<1273:SOCTSS>2.0.CO;2.

Gulev, S. K., and K. Belyaev, 2012: Probability distribution characteristics for surface air–sea turbulent heat fluxes over the global ocean. *J. Climate*, **25**, 184–206, https://doi.org/10.1175/2011JCLI4211.1.

——, O. Zolina, and S. Grigoriev, 2001: Extratropical cyclone variability in the Northern Hemisphere winter from the NCEP/NCAR reanalysis data. *Climate Dyn.*, **17**, 795–809, https://doi.org/10.1007/s003820000145.

——, T. Jung, and E. Ruprecht, 2002: Climatology and Interannual Variability in the Intensity of Synoptic-Scale Processes in the North Atlantic from the NCEP–NCAR Reanalysis Data. *J. Climate*, **15**, 809–828, https://doi.org/10.1175/1520-0442(2002)015<0809:CAIVIT>2.0.CO;2.

——, ——, and ——, 2007: Estimation of the impact of sampling errors in the VOS observations on air–sea fluxes. Part II: Impact on trends and interannual variability. *J. Climate*, **20**, 302–315, https://doi.org/10.1175/JCLI4008.1.

——, M. Latif, N. Keenlyside, W. Park, and K. P. Koltermann, 2013: North Atlantic Ocean control on surface heat flux on multi-decadal timescales. *Nature*, **499**, 464–467, https://doi.org/10.1038/nature12268.

Hand, R., N. Keenlyside, N.-E. Omrani, and M. Latif, 2014: Simulated response to inter-annual SST variations in the Gulf Stream region. *Climate Dyn.*, **42**, 715–731, https://doi.org/10.1007/s00382-013-1715-y.

Harden, B. E., I. A. Renfrew, and G. N. Petersen, 2015: Meteorological buoy observations from the central Iceland Sea. *J. Geophys. Res. Atmos.*, **120**, 3199–3208, https://doi.org/10.1002/2014JD022584.

Harman, J. R., 1987: Mean monthly North American anticyclone frequencies, 1950–79. *Mon. Wea. Rev.*, **115**, 2840–2848, https://doi.org/10.1175/1520-0493(1987)115<2840:MMNAAF>2.0.CO;2.

Hersbach, H., and D. P. Dee, 2016: ERA5 reanalysis is in production. *ECMWF Newletter*, No. 147, ECMWF, Reading, United Kingdom, p. 7, https://www.ecmwf.int/sites/default/files/elibrary/2016/16299-newsletter-no147-spring-2016.pdf.

Hodges, K. I., B. J. Hoskins, J. Boyle, and C. Thorncroft, 2003: A comparison of recent reanalysis datasets using objective feature tracking: Storm tracks and tropical easterly waves. *Mon. Wea. Rev.*, **131**, 2012–2037, https://doi.org/10.1175/1520-0493(2003)131<2012:ACORRD>2.0.CO;2.

——, R. W. Lee, and L. Bengtsson, 2011: A comparison of extratropical cyclones in recent reanalyses ERA-Interim, NASA MERRA, NCEP CFSR, and JRA-25. *J. Climate*, **24**, 4888–4906, https://doi.org/10.1175/2011JCLI4097.1.

Holdsworth, A. M., and P. G. Myers, 2015: The influence of high-frequency atmospheric forcing on the circulation and deep convection of the Labrador Sea. *J. Climate*, **28**, 4980–4996, https://doi.org/10.1175/JCLI-D-14-00564.1.

Ioannidou, L., and M. K. Yau, 2008: A climatology of the Northern Hemisphere winter anticyclones. *J. Geophys. Res.*, **113**, D08119, https://doi.org/10.1029/2007JD008409.

Iwasaka, N., and J. M. Wallace, 1995: Large scale air-sea interaction in the Northern Hemisphere from the viewpoint of variations in surface heat flux from SVD analysis. *J. Meteor. Soc. Japan*, **73**, 781–794, https://doi.org/10.2151/jmsj1965.73.4_781.

Iwasaki, T., T. Shoji, Y. Kanno, M. Sawada, M. Ujiie, and K. Takaya, 2014: Isentropic analysis of polar cold airmass streams in the Northern Hemispheric winter. *J. Atmos. Sci.*, **71**, 2230–2243, https://doi.org/10.1175/JAS-D-13-058.1.

Jung, T., M. Hilmer, E. Ruprecht, S. Kleppek, S. K. Gulev, and O. Zolina, 2003: Characteristics of the recent eastward shift of interannual NAO variability. *J. Climate*, **16**, 3371–3382, https://doi.org/10.1175/1520-0442(2003)016<3371:COTRES>2.0.CO;2.

——, S. K. Gulev, I. Rudeva, and V. Soloviov, 2006: Sensitivity of extratropical cyclone characteristics to horizontal resolution in the ECMWF model. *Quart. J. Roy. Meteor. Soc.*, **132**, 1839–1857, https://doi.org/10.1256/qj.05.212.

Kim, W. M., S. Yeager, P. Chang, and G. Danabasoglu, 2016: Atmospheric conditions associated with Labrador Sea deep convection: New insights from a case study of the 2006/07 and 2007/08 winters. *J. Climate*, **29**, 5281–5297, https://doi.org/10.1175/JCLI-D-15-0527.1.

King, M. L., P. J. Smith, and A. R. Lupo, 1995: A diagnosis of the development of a winter anticyclone over North America. *Mon. Wea. Rev.*, **123**, 2273–2284, https://doi.org/10.1175/1520-0493(1995)123<2273:ADOTDO>2.0.CO;2.

Kolstad, E. W., T. J. Bracegirdle, and I. A. Seierstad, 2009: Marine cold-air outbreaks in the North Atlantic: Temporal distribution and associations with large-scale atmospheric circulation. *Climate Dyn.*, **33**, 187–197, https://doi.org/10.1007/s00382-008-0431-5.

Konda, M., H. Ichikawa, H. Tomita, and M. F. Cronin, 2010: Surface heat flux variations across the Kuroshio Extension as observed by surface flux buoys. *J. Climate*, **23**, 5206–5221, https://doi.org/10.1175/2010JCLI3391.1.

Kravtsov, S., and S. K. Gulev, 2013: Kinematics of eddy–mean flow interaction in an idealized atmospheric model. *J. Atmos. Sci.*, **70**, 2574–2595, https://doi.org/10.1175/JAS-D-12-0309.1.

——, N. Tilinina, Y. Zyulyaeva, and S. K. Gulev, 2016: Empirical modeling and stochastic simulation of sea level pressure variability. *J. Appl. Meteor. Climatol.*, **55**, 1197–1219, https://doi.org/10.1175/JAMC-D-15-0186.1.

Kuwano-Yoshida, A., and Y. Asuma, 2008: Numerical study of explosively developing extratropical cyclones in the northwestern Pacific region. *Mon. Wea. Rev.*, **136**, 712–740, https://doi.org/10.1175/2007MWR2111.1.

——, and T. Enomoto, 2013: Predictability of explosive cyclogenesis over the northwestern Pacific region using ensemble reanalysis. *Mon. Wea. Rev.*, **141**, 3769–3785, https://doi.org/10.1175/MWR-D-12-00161.1.

——, and S. Minobe, 2017: Storm-track response to SST fronts in the northwestern Pacific region in an AGCM. *J. Climate*, **30**, 1081–1102, https://doi.org/10.1175/JCLI-D-16-0331.1.

——, ——, and S.-P. Xie, 2010: Precipitation response to the Gulf Stream in an atmospheric GCM. *J. Climate*, **23**, 3676–3698, https://doi.org/10.1175/2010JCLI3261.1.

Kwon, Y.-O., M. A. Alexander, N. A. Bond, C. Frankignoul, H. Nakamura, B. Qiu, and L. A. Thompson, 2010: Role of the Gulf Stream and Kuroshio–Oyashio systems in large-scale atmosphere–ocean interaction: A review. *J. Climate*, **23**, 3249–3281, https://doi.org/10.1175/2010JCLI3343.1.

Large, W., and S. G. Yeager, 2009: The global climatology of an interannually varying air–sea flux data set. *Climate Dyn.*, **33**, 341–364, https://doi.org/10.1007/s00382-008-0441-3.

Löptien, U., O. Zolina, S. Gulev, M. Latif, and V. Soloviov, 2008: Cyclone life cycle characteristics over the Northern Hemisphere in coupled GCMs. *Climate Dyn.*, **31**, 507–532, https://doi.org/10.1007/s00382-007-0355-5.

Lupo, A. R., P. J. Smith, and P. Zwack, 1992: A diagnosis of the explosive development of two extratropical cyclones. *Mon. Wea. Rev.*, **120**, 1490–1523, https://doi.org/10.1175/1520-0493(1992)120<1490:ADOTED>2.0.CO;2.

Ma, X., and Coauthors, 2015a: Distant influence of Kuroshio eddies on North Pacific weather patterns? *Sci. Rep.*, **5**, 17785, https://doi.org/10.1038/srep17785.

——, P. Chang, R. Saravanan, D. Wu, X. Lin, L. Wu, and X. Wan, 2015b: Winter extreme flux events in the Kuroshio and Gulf Stream extension regions and relationship with modes of North Pacific and Atlantic variability. *J. Climate*, **28**, 4950–4970, https://doi.org/10.1175/JCLI-D-14-00642.1.

Mailier, P. J., D. B. Stephenson, C. A. T. Ferro, and K. I. Hodges, 2006: Serial clustering of extratropical cyclones. *Mon. Wea. Rev.*, **134**, 2224–2240, https://doi.org/10.1175/MWR3160.1.

Meindl, E. A., and G. D. Hamilton, 1992: Programs of the national data buoy center. *Bull. Amer. Meteor. Soc.*, **73**, 985–993, https://doi.org/10.1175/1520-0477(1992)073<0985:POTNDB>2.0.CO;2.

Minobe, S., A. Kuwano-Yoshida, N. Komori, S.-P. Xie, and R. J. Small, 2008: Influence of the Gulf Stream on the troposphere. *Nature*, **452**, 206–209, https://doi.org/10.1038/nature06690.

——, M. Miyashita, A. Kuwano-Yoshida, H. Tokinaga, and S.-P. Xie, 2010: Atmospheric response to the Gulf Stream: Seasonal variations. *J. Climate*, **23**, 3699–3719, https://doi.org/10.1175/2010JCLI3359.1.

Moore, G. W. K., and I. A. Renfrew, 2002: An assessment of the surface turbulent heat fluxes from the NCEP–NCAR reanalysis over the western boundary currents. *J. Climate*, **15**, 2020–2037, https://doi.org/10.1175/1520-0442(2002)015<2020:AAOTST>2.0.CO;2.

——, R. S. Pickart, I. A. Renfrew, and K. Våge, 2014: What causes the location of the air-sea turbulent heat flux maximum over the Labrador Sea? *Geophys. Res. Lett.*, **41**, 3628–3635, https://doi.org/10.1002/2014GL059940.

——, I. A. Renfrew, B. E. Harden, and S. H. Mernild, 2015: The impact of resolution on the representation of southeast

Greenland barrier winds and katabatic flows. *Geophys. Res. Lett.*, **42**, 3011–3018, https://doi.org/10.1002/2015GL063550.

Nakamura, H., T. Sampe, Y. Tanimoto, and A. Shimpo, 2004: Observed associations among storm tracks, jet streams and midlatitude oceanic fronts. *Earth's Climate: The Ocean–Atmosphere Interaction*, *Geophys. Monogr.*, Vol. 147, Amer. Geophys. Union, 329–345, https://doi.org/10.1029/147GM18.

——, A. Nishina, and S. Minobe, 2012: Response of storm tracks to bimodal Kuroshio path states south of Japan. *J. Climate*, **25**, 7772–7779, https://doi.org/10.1175/JCLI-D-12-00326.1.

Naud, C., J. Booth, M. Lebsock, and M. Grecu, 2018: Observational constraint for precipitation in extratropical cyclones: Sensitivity to data sources. *J. Appl. Meteor. Climatol.*, **57**, 991–1009, https://doi.org/10.1175/JAMC-D-17-0289.1.

Neiman, P. J., and M. A. Shapiro, 1993: The life cycle of an extratropical marine cyclone. Part I: Frontal-cyclone evolution and thermodynamic air-sea interaction. *Mon. Wea. Rev.*, **121**, 2153–2176, https://doi.org/10.1175/1520-0493(1993)121<2153:TLCOAE>2.0.CO;2.

Neu, U., and Coauthors, 2013: IMILAST: A community effort to intercompare extratropical cyclone detection and tracking algorithms. *Bull. Amer. Meteor. Soc.*, **94**, 529–547, https://doi.org/10.1175/BAMS-D-11-00154.1.

Nieto Ferreira, R., and L. Hall, 2015: Midlatitude cyclones in the southeastern United States: Frequency and structure differences by cyclogenesis region. *Int. J. Climatol.*, **35**, 3798–3811, https://doi.org/10.1002/joc.4247.

Ogawa, F., H. Nakamura, K. Nishii, T. Miyasaka, and A. Kuwano-Yoshida, 2012: Dependence of the climatological axial latitudes of the tropospheric westerlies and storm tracks on the latitude of an extratropical oceanic front. *Geophys. Res. Lett.*, **39**, L05804, https://doi.org/10.1029/2011GL049922.

O'Reilly, C. H., and A. Czaja, 2015: The response of the Pacific storm track and atmospheric circulation to Kuroshio Extension variability. *Quart. J. Roy. Meteor. Soc.*, **141**, 52–66, https://doi.org/10.1002/qj.2334.

——, S. Minobe, A. Kuwano-Yoshida, and T. Woollings, 2017: The Gulf Stream influence on wintertime North Atlantic jet variability. *Quart. J. Roy. Meteor. Soc.*, **143**, 173–183, https://doi.org/10.1002/qj.2907.

Papritz, L., 2017: Synoptic environments and characteristics of cold air outbreaks in the Irminger Sea. *Int. J. Climatol.*, **37**, 193–207, https://doi.org/10.1002/joc.4991.

——, and T. Spengler, 2015: Analysis of the slope of isentropic surfaces and its tendencies over the North Atlantic. *Quart. J. Roy. Meteor. Soc.*, **141**, 3226–3238, https://doi.org/10.1002/qj.2605.

——, and ——, 2017: A Lagrangian climatology of wintertime cold air outbreaks in the Irminger and Nordic seas and their role in shaping air–sea heat fluxes. *J. Climate*, **30**, 2717–2737, https://doi.org/10.1175/JCLI-D-16-0605.1.

——, S. Pfahl, H. Sodemann, and H. Wernli, 2015: A climatology of cold air outbreaks and their impact on air–sea heat fluxes in the high-latitude South Pacific. *J. Climate*, **28**, 342–364, https://doi.org/10.1175/JCLI-D-14-00482.1.

Parfitt, R., and A. Czaja, 2016: On the contribution of synoptic transients to the mean atmospheric state in the Gulf Stream region. *Quart. J. Roy. Meteor. Soc.*, **142**, 1554–1561, https://doi.org/10.1002/qj.2689.

——, ——, S. Minobe, and A. Kuwano-Yoshida, 2016: The atmospheric frontal response to SST perturbations in the Gulf Stream region. *Geophys. Res. Lett.*, **43**, 2299–2306, https://doi.org/10.1002/2016GL067723.

——, ——, and Y.-O. Kwon, 2017: The impact of SST resolution change in the ERA-Interim reanalysis on wintertime Gulf Stream frontal air–sea interaction. *Geophys. Res. Lett.*, **44**, 3246–3254, https://doi.org/10.1002/2017GL073028.

Patoux, J., X. Yuan, and C. Li, 2009: Satellite-based midlatitude cyclone statistics over the Southern Ocean: 1. Scatterometer-derived pressure fields and storm tracking. *J. Geophys. Res.*, **114**, D04105, https://doi.org/10.1029/2008JD010873.

Pfahl, S., E. Madonna, M. Boettcher, H. Joos, and H. Wernli, 2014: Warm conveyor belts in the ERA-Interim dataset (1979–2010). Part II: Moisture origin and relevance for precipitation. *J. Climate*, **27**, 27–40, https://doi.org/10.1175/JCLI-D-13-00223.1.

Pinto, J. G., S. Zacharias, A. H. Fink, G. C. Leckebusch, and U. Ulbrich, 2009: Factors contributing to the development of extreme North Atlantic cyclones and their relationship with the NAO. *Climate Dyn.*, **32**, 711–737, https://doi.org/10.1007/s00382-008-0396-4.

——, N. Bellenbaum, M. K. Karremann, and P. M. Della-Marta, 2013: Serial clustering of extratropical cyclones over the North Atlantic and Europe under recent and future climate conditions. *J. Geophys. Res. Atmos.*, **118**, 12 476–12 485, https://doi.org/10.1002/2013JD020564.

Rancic, M., J. C. Derber, D. Parrish, R. Treadon, and D. T. Kleist, 2008: The development of the First-Order Time extrapolation to the Observation (FOTO) method and its application in the NCEP global data assimilation system. *12th Symp. on Integrated Observing and Assimilation Systems for the Atmosphere, Oceans, and Land Surface (IOAS-AOLS)*, New Orleans, LA, Amer. Meteor. Soc., J6.1, https://ams.confex.com/ams/pdfpapers/131816.pdf.

Reed, T. R., 1933: The North American high-level anticyclone. *Mon. Wea. Rev.*, **61**, 321–325, https://doi.org/10.1175/1520-0493(1933)61<321:TNAHA>2.0.CO;2.

——, 1937: Further observations on the North American high-level anticyclone. *Mon. Wea. Rev.*, **65**, 364–366, https://doi.org/10.1175/1520-0493(1937)65<364b:FOOTNA>2.0.CO;2.

Renfrew, I. A., G. W. K. Moore, P. S. Guest, and K. Bumke, 2002: A comparison of surface layer and surface turbulent flux observations over the Labrador Sea with ECMWF analyses and NCEP reanalyses. *J. Phys. Oceanogr.*, **32**, 383–400, https://doi.org/10.1175/1520-0485(2002)032<0383:ACOSLA>2.0.CO;2.

Roberts, J. B., F. R. Robertson, C. A. Clayson, and M. G. Bosilovich, 2012: Characterization of turbulent latent and sensible heat flux exchange between the atmosphere and ocean in MERRA. *J. Climate*, **25**, 821–838, https://doi.org/10.1175/JCLI-D-11-00029.1.

Rudeva, I., and S. K. Gulev, 2007: Climatology of cyclone size characteristics and their changes during the cyclone life cycle. *Mon. Wea. Rev.*, **135**, 2568–2587, https://doi.org/10.1175/MWR3420.1.

——, and ——, 2011: Composite analysis of North Atlantic extratropical cyclones in NCEP–NCAR reanalysis data. *Mon. Wea. Rev.*, **139**, 1419–1446, https://doi.org/10.1175/2010MWR3294.1.

——, S. Gulev, I. Simmonds, and N. Tilinina, 2014: The sensitivity of characteristics of cyclone activity to identification procedures in tracking algorithms. *Tellus*, **66A**, 24961, https://doi.org/10.3402/tellusa.v66.24961.

Saha, S., and Coauthors, 2010: The NCEP Climate Forecast System Reanalysis. *Bull. Amer. Meteor. Soc.*, **91**, 1015–1057, https://doi.org/10.1175/2010BAMS3001.1.

Sanders, F., and J. R. Gyakum, 1980: Synoptic-dynamic climatology of the "bomb." *Mon. Wea. Rev.*, **108**, 1589–1606, https://doi.org/10.1175/1520-0493(1980)108<1589:SDCOT>2.0.CO;2.

Sasaki, Y. N., S. Minobe, T. Asai, and M. Inatsu, 2012: Influence of the Kuroshio in the East China Sea on the early summer (baiu) rain. *J. Climate*, **25**, 6627–6645, https://doi.org/10.1175/JCLI-D-11-00727.1.

Schemm, S., I. Rudeva, and I. Simmonds, 2015: Extratropical fronts in the lower troposphere—Global perspectives obtained from two automated methods. *Quart. J. Roy. Meteor. Soc.*, **141**, 1686–1698, https://doi.org/10.1002/qj.2471.

Semmler, T., L. Stulic, T. Jung, N. Tilinina, C. Campos, S. Gulev, and D. Koracin, 2016: Seasonal atmospheric responses to reduced Arctic sea ice in an ensemble of coupled model simulations. *J. Climate*, **29**, 5893–5913, https://doi.org/10.1175/JCLI-D-15-0586.1.

Serreze, M. C., and A. P. Barrett, 2011: Characteristics of the Beaufort Sea high. *J. Climate*, **24**, 159–182, https://doi.org/10.1175/2010JCLI3636.1.

Shaman, J., R. M. Samelson, and E. Skyllingstad, 2010: Air–sea fluxes over the Gulf Stream region: Atmospheric controls and trends. *J. Climate*, **23**, 2651–2670, https://doi.org/10.1175/2010JCLI3269.1.

Shoji, T., Y. Kanno, T. Iwasaki, and K. Takaya, 2014: An isentropic analysis of the temporal evolution of East Asian cold air outbreaks. *J. Climate*, **27**, 9337–9348, https://doi.org/10.1175/JCLI-D-14-00307.1.

Small, R. J., and Coauthors, 2008: Air–sea interaction over ocean fronts and eddies. *Dyn. Atmos. Oceans*, **45**, 274–319, https://doi.org/10.1016/j.dynatmoce.2008.01.001.

——, R. A. Tomas, and F. O. Bryan, 2014: Storm track response to ocean fronts in a global high-resolution climate model. *Climate Dyn.*, **43**, 805–828, https://doi.org/10.1007/s00382-013-1980-9.

Tan, Y.-C., and J. A. Curry, 1993: A diagnostic study of the evolution of an intense North American anticyclone during winter 1989. *Mon. Wea. Rev.*, **121**, 961–975, https://doi.org/10.1175/1520-0493(1993)121<0961:ADSOTE>2.0.CO;2.

Tanimoto, Y., H. Nakamura, T. Kagimoto, and S. Yamane, 2003: An active role of extratropical sea surface temperature anomalies in determining anomalous turbulent heat flux. *J. Geophys. Res.*, **108**, 3304, https://doi.org/10.1029/2002JC001750.

Tilinina, N., S. K. Gulev, I. Rudeva, and P. Koltermann, 2013: Comparing cyclone life cycle characteristics and their interannual variability in different reanalyses. *J. Climate*, **26**, 6419–6438, https://doi.org/10.1175/JCLI-D-12-00777.1.

——, ——, and D. H. Bromwich, 2014: New view of Arctic cyclone activity from the Arctic system reanalysis. *Geophys. Res. Lett.*, **41**, 1766–1772, https://doi.org/10.1002/2013GL058924.

Ulbrich, U., and Coauthors, 2013: Are greenhouse gas signals of Northern Hemisphere winter extra-tropical cyclone activity dependent on the identification and tracking algorithm? *Meteor. Z.*, **22**, 61–68, https://doi.org/10.1127/0941-2948/2013/0420.

Vannière, B., A. Czaja, and H. F. Dacre, 2017: Contribution of the cold sector of extratropical cyclones to mean state features over the Gulf Stream in winter. *Quart. J. Roy. Meteor. Soc.*, **143**, 1990–2000, https://doi.org/10.1002/qj.3058.

Visbeck, M., E. P. Chassignet, R. G. Curry, T. L. Delworth, R. R. Dickson, and G. Krahmann, 2003: The ocean's response to North Atlantic Oscillation variability. *The North Atlantic Oscillation: Climatic Significance and Environmental Impact*, *Geophys. Monogr.*, Vol. 134, Amer. Geophys. Union, 113–145, https://doi.org/10.1029/134GM06.

Wiedenmann, J. M., A. R. Lupo, I. I. Mokhov, and E. A. Tikhonova, 2002: The climatology of blocking anticyclones for the Northern and Southern Hemispheres: Block intensity as a diagnostic. *J. Climate*, **15**, 3459–3473, https://doi.org/10.1175/1520-0442(2002)015<3459:TCOBAF>2.0.CO;2.

Wilson, A. B., D. H. Bromwich, and K. M. Hines, 2012: Evaluation of Polar WRF forecasts on the Arctic System Reanalysis Domain: 2. Atmospheric hydrologic cycle. *J. Geophys. Res.*, **117**, D04107, https://doi.org/10.1029/2011JD016765.

Woollings, T., L. Papritz, C. Mbengue, and T. Spengler, 2016: Diabatic heating and jet stream shifts: A case study of the 2010 negative North Atlantic Oscillation winter. *Geophys. Res. Lett.*, **43**, 9994–10 002, https://doi.org/10.1002/2016GL070146.

Yau, M. K., and M. Jean, 1989: Synoptic aspects and physical processes in the rapidly intensifying cyclone of 6–8 March 1986. *Atmos.–Ocean*, **27**, 59–86, https://doi.org/10.1080/07055900.1989.9649328.

Yu, L., and R. A. Weller, 2007: Objectively analyzed air–sea heat fluxes for the global ice-free oceans (1981–2005). *Bull. Amer. Meteor. Soc.*, **88**, 527–539, https://doi.org/10.1175/BAMS-88-4-527.

Yuan, X., J. Patoux, and C. Li, 2009: Satellite-based midlatitude cyclone statistics over the Southern Ocean: 2. Tracks and surface fluxes. *J. Geophys. Res.*, **114**, D04106, https://doi.org/10.1029/2008JD011190.

Zhao, Y. P., and G. A. McBean, 1986: Annual and interannual variability of the North Pacific ocean-to-atmosphere total heat transfer. *Atmos.–Ocean*, **24**, 265–282, https://doi.org/10.1080/07055900.1986.9649251.

Zishka, K. M., and P. J. Smith, 1980: The climatology of cyclones and anticyclones over North America and surrounding ocean environs for January and July, 1950–77. *Mon. Wea. Rev.*, **108**, 387–401, https://doi.org/10.1175/1520-0493(1980)108<0387:TCOCAA>2.0.CO;2.

Zolina, O., and S. K. Gulev, 2002: Improving the accuracy of mapping cyclone numbers and frequencies. *Mon. Wea. Rev.*, **130**, 748–759, https://doi.org/10.1175/1520-0493(2002)130<0748:ITAOMC>2.0.CO;2.

——, and ——, 2003: Synoptic variability of ocean–atmosphere turbulent fluxes associated with atmospheric cyclones. *J. Climate*, **16**, 2717–2734, https://doi.org/10.1175/1520-0442(2003)016<2717:SVOOTF>2.0.CO;2.